

Dynamic Evolution of Palladium Single Atoms on Anatase Titania Support Determines the Reverse Water-Gas Shift Activity

Linxiao Chen,¹ Sarah I. Allec,¹ Manh-Thuong Nguyen,¹ Libor Kovarik,¹ Adam S. Hoffman,² Jiyun Hong,² Debora Meira,³ Honghong Shi,¹ Simon R. Bare,² Vassiliki-Alexandra Glezakou,^{1,4} Roger Rousseau,^{1,4} and János Szanyi^{1*}

1 Pacific Northwest National Laboratory, Richland, WA 99352, USA

2 Stanford Synchrotron Radiation Lightsource, SLAC National Accelerator Laboratory, Menlo Park, CA 94025, USA

3 Canadian Light Source Inc., 44 Innovation Boulevard, Saskatoon, Saskatchewan S7N 2V3, Canada

4 Present address: Oak Ridge National Laboratory, Oak Ridge, TN 37830, USA

*Corresponding author: janos.szanyi@pnnl.gov

Abstract

Research interest in single-atom catalysts (SACs) has been continuously rising. However, the lack of understanding of the dynamic behaviors of SACs during applications hinder catalyst development and mechanistic understanding. Herein, we report on the evolution of active sites over Pd/TiO₂-anatase SAC (Pd₁/TiO₂) in the reverse water-gas shift (rWGS) reaction. Combining kinetics, *in-situ* characterization, and theory, we show that at $T \geq 350$ °C, the reduction of TiO₂ by H₂ alters the coordination environment of Pd, creating Pd sites with partially cleaved Pd–O interfacial bonds and a unique electronic structure that exhibit high intrinsic rWGS activity through the carboxyl pathway. The activation by H₂ is accompanied by the partial sintering of single Pd atoms (Pd₁) into disordered, flat, ~1 nm diameter clusters (Pd_n). The highly active Pd sites in the new coordination environment under H₂ are eliminated by oxidation, which, when performed at high temperature, also re-disperses Pd_n and facilitates the reduction of TiO₂. In contrast, Pd₁ sinters into crystalline, ~5 nm particles (Pd_{NP}) during CO treatment, deactivating Pd₁/TiO₂. During the rWGS reaction, the two Pd evolution pathways co-exist. The activation by H₂ dominates, leading to the increasing rate with time-on-stream, and steady-state Pd active sites similar with the ones formed under H₂. This work demonstrates how the coordination environment and nuclearity of metal sites on a SAC evolve during catalysis and pre-treatments, and how their activity is modulated by these behaviors. These insights on SAC dynamics and structure-function relationship are valuable to mechanistic understanding and catalyst design.

Keywords: single-atom catalysis, palladium, anatase titania, water-gas shift, metal-oxide interface

Introduction

The past decade has witnessed the explosion of research on atomically dispersed metal catalysts, or “single-atom catalysts (SACs)”. The interest is driven by the desire to reach the high metal utilization efficiency and site uniformity of homogeneous catalysts on the durable, process-friendly heterogeneous platforms.¹⁻³ The extensive efforts delivered significant progress in the areas of synthesis,⁴⁻⁸ characterization,⁹⁻¹¹ applications,¹²⁻¹⁹ and mechanistic insights.²⁰⁻²² Despite the advances, an enduring issue haunting related research is the complicated dynamics of SACs. Because single metal atoms are only bound to binding motifs offered by the support, compared to metal nanoparticles, they are often less stable, and their properties are more sensitive to changes in the support and the metal-support interface (MSI).²³⁻²⁶ As a result, the structural and electronic properties of SACs often respond to the reaction and/or pre-treatment conditions drastically, which can profoundly affect catalysis.^{21, 24, 27-29} Understanding these behaviors is necessary for developing stable SACs for applications under harsh conditions, as well as accurately identifying active sites, reaction mechanisms, and structure-function relationship.

Despite their importance, the dynamics of SACs and their catalytic consequences are often neglected or difficult to reveal. The characterization of SACs is challenging, and it needs to be conducted *in-situ* to accurately correlate it with kinetic data.⁹⁻¹¹ Besides, the “site uniformity” on SACs is more of a wish than reality,³⁰⁻³² due to the presence of various binding sites on supports, the high mobility of single metal atoms, and changes in the support structure during catalysis.³³⁻³⁵ Different types of sites and their roles in catalysis are hard to deconvolute as most spectroscopic techniques yield ensemble-average information. Thus, reliable experimental insights about catalyst dynamics, actual active sites, and structure-function relationships on SACs are rare,^{17, 21, 23, 24, 27-29, 36-38} impeding the understanding of reaction chemistry and rational catalyst design.

In this work, we investigated the dynamic structural evolution of a Pd/TiO₂-anatase SAC and its impacts on the reverse water-gas shift (rWGS) reaction, i.e., CO₂ hydrogenation to CO. The rWGS has sparked significant interests for both practical and fundamental reasons,³⁹⁻⁴³ and mechanistic studies predicted SACs to be ideal for this reaction.^{39, 44} Combining detailed kinetics, comprehensive *in-situ* characterization, and theoretical modelling, we revealed the formation of Pd sites with high intrinsic activity during the reaction. This is achieved through the reduction of TiO₂ by H₂, leading to Pd sites with unique electronic structure and partially cleaved MSI, which are particularly effective in the carboxyl pathway of the rWGS. Oxidation eliminates these highly active Pd sites by reversing these coordination environment changes. In contrast, reducing the SAC with CO leads to the severe sintering of single Pd atoms (Pd_I), and thus the loss of rWGS active sites and, consequently, activity. The comprehensive insights offered by this work on single-atom catalysis are rare in the literature, and instructive for the rational design of SACs.

Results

1. Changes in the rWGS rate on Pd₁/TiO₂: activation by H₂ and deactivation by CO

Pd/TiO₂-anatase SACs (herein referred to as “Pd₁/TiO₂”; “TiO₂” and “TiO₂-A” both refer to anatase TiO₂) were synthesized by strong electrostatic adsorption.⁷ The atomic dispersion of Pd on 0.0125 wt% (loading verified by ICP) Pd₁/TiO₂ was confirmed by the results of high-angle annular dark-field scanning transmission electron microscopy (HAADF-STEM), X-ray absorption spectroscopy (XAS), and CO adsorption IR (CO-IR) measurements, which will be shown later. XAS also shows the atomic dispersion of Pd at ≤ 0.05 wt% loading (Figure S2). In CO₂ hydrogenation at 400 °C under ambient pressure, all Pd₁/TiO₂ with different Pd loadings exhibit > 99% selectivity towards CO (reverse water-gas shift, rWGS, < 10% CO₂ conversion), as expected on highly dispersed noble metal catalysts.^{40, 45-47} Interestingly, we observed a slow (in ~25 h), gradual, two-fold increase in the rWGS rate per Pd with time-on-stream (TOS) on ≤ 0.025 wt% Pd₁/TiO₂ (purple, red, and green in Figure 1a). Since anatase is stable at 400 °C,⁴⁸ the rate increase is not caused by support phase change. Since the Pd is atomically dispersed on fresh Pd₁/TiO₂, the rate increase cannot be due to higher Pd dispersion, i.e., more peripheral Pd sites that contribute to the majority of the rWGS activity,^{39, 44} either. Therefore, it reflects higher intrinsic activity of Pd. In contrast, less dispersed Pd/TiO₂, synthesized by incipient wetness impregnation (0.025 or 0.8 wt% Pd), or 0.05 wt% Pd₁/TiO₂ do not show the phenomenon (brown, black, and blue symbols, respectively, in Figure 1a; dilution with pristine TiO₂ has no effect, Figure S3), indicating that the increase in intrinsic activity can only be observed when Pd is highly, if not atomically dispersed, and at very low surface coverage (1 Pd₁ per ~120 nm² TiO₂ surface at 0.025 wt% loading).

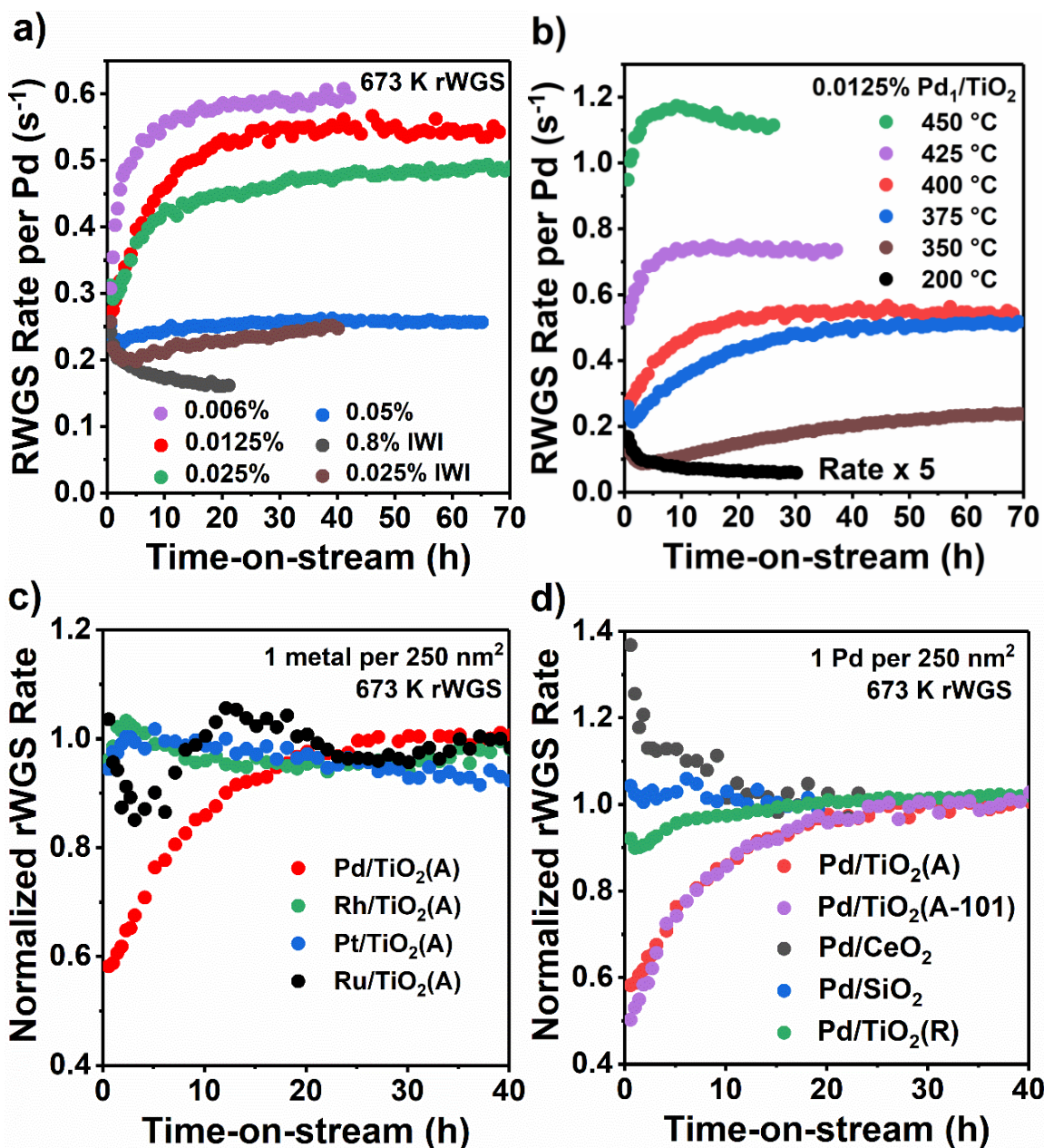


Figure 1. Variations in the rWGS rate per Pd with TOS at 400 °C: **a)** Pd/TiO₂ of various Pd loadings by wt%: 0.006 (purple), 0.0125 (red), 0.025 (green), 0.05 (blue), 0.025 synthesized by IWI (brown), and 0.8 (IWI, black); **b)** 0.0125 wt% Pd₁/TiO₂ at various temperatures: 450 (green), 425 (purple), 400 (red), 375 (blue), 350 (brown), and 200 °C (black, rate multiplied by 5); **c)** (normalized to the final rate) various noble metals supported on anatase TiO₂: Pd (red), Rh (green), Pt (blue), and Ru (black); **d)** (normalized to the final rate) Pd supported on various oxides: anatase (red), anatase with > 90% (101) surfaces (purple), CeO₂ (black), SiO₂ (blue), and rutile (green). All catalysts in panels **c)** and **d)** share noble metal coverage and synthesis method with 0.0125 wt% Pd₁/TiO₂, and near-atomic dispersion is expected (atomic dispersion of Pt/TiO₂ reported).³⁷ Absolute rates are reported in Table S1. Typical reaction conditions: 50 mg catalyst, $T = 400$ °C, H₂ : CO : He = 4 : 1 : 5, total flow = 10 SCCM, 1 atm. The rate on pristine TiO₂ was subtracted.

To understand the intrinsic activity increase, we tested the rWGS on 0.0125 wt% Pd₁/TiO₂ (used in all experiments below) at various temperatures. Figure 1b shows that the rate increases with TOS at $T \geq 350$ °C, but at 350 (brown) and 375 °C (blue), it drops first before it increases. In contrast, at 200 °C (black), the rate decreases monotonically with TOS, presumably due to sintering. Thus, the activation of Pd₁/TiO₂ requires high temperature, consistent with its high apparent activation barrier of ~120 kJ/mol (Figure S4, obtained by modelling data in Figure 1b). We also tested Pd/CeO₂, Pd/SiO₂, Pd/TiO₂-rutile (“TiO₂-R”), Pt/TiO₂ (atomically dispersed³⁷), Rh/TiO₂, and Ru/TiO₂, with the same synthesis procedure and noble metal coverage consistent with 0.0125 wt% Pd₁/TiO₂. Figures 1c-d show that none of other highly dispersed M/M'_xO_y catalysts show increasing rate with TOS, i.e., the intrinsic activity increase is unique to Pd₁/TiO₂-A, implying that it involves specific metal-support interaction. Particularly, the absence of the phenomenon on CeO₂ and TiO₂-R, on which surface oxygen vacancies (O_v) are more favored than on TiO₂-A,⁴⁹⁻⁵² suggests that it is not due to surface O_v directly participating in the rWGS. Note that we also tested Pd on a faceted TiO₂-A with > 90% exposed surfaces as (101) orientation, the most stable surface of anatase (see Figure S5 for TEM images).^{51, 53-55} It exhibits identical rate trend (purple in Figure 1d) with Pd₁/TiO₂ (red), indicating that the (101) surface is an appropriate model for TiO₂-A for the theoretical modelling study below.

The rWGS stream exiting the reactor comprises of 40% H₂, 10% CO₂, ~5000 ppm CO and H₂O (from ~5% CO₂ conversion). As a first step to reveal the physical origin of the intrinsic activity increase, the effects of each component of the gas stream were deconvoluted. In the first 15 h, we replaced the rWGS stream with 40% H₂, 5000 ppm CO, or 40% H₂ + 5000 ppm CO at 400 °C (H₂ and CO concentrations equal to those in the rWGS stream), and switched to the rWGS stream at $t = 15$ h. Figure 2a shows that the H₂ + CO mixture (blue) has identical impact on the

activity of Pd₁/TiO₂ with the rWGS stream (red). In comparison, Pd₁/TiO₂ becomes more active under H₂ alone (green), and less active under CO alone (black). The results imply that H₂ causes the intrinsic activity increase, while CO deactivates the catalyst. During the rWGS, H₂ and CO function in parallel. Thus, H₂ + CO in He exactly replicates the effects of the rWGS stream, and we deduce that H₂O and CO₂ in the reaction stream have no or minimal effects. To verify this observation, we varied the CO concentration in the rWGS stream either by adding CO or by reducing the amount of catalyst and thus CO₂ conversion. Figure 2b shows that the final per-Pd rate is negatively correlated with CO concentration, supporting the deactivating effect of CO. In addition, we pre-treated Pd₁/TiO₂ with H₂ or CO at 400 °C (referred to as “H400” and “CO400” Pd₁/TiO₂, respectively, with higher concentration and/or time to ensure the complete evolution of Pd). Figure 2c shows that the initial rate on H400 Pd₁/TiO₂ (green) is higher than the final rate on the fresh catalyst (red), and the rate drops with TOS when the rWGS stream, and thus CO, is introduced. In contrast, CO400 Pd₁/TiO₂ (black) shows lower initial rate and minimal rate increase compared to the fresh catalyst. The results further verify that H₂ and CO activates and deactivates Pd₁/TiO₂, respectively. When CO concentration is very low (green in Figure 2b), i.e., the deactivation by CO is negligible, the final rate on fresh Pd₁/TiO₂ is close to the initial rate on H400 Pd₁/TiO₂ (green in Figure 2c, both ~1.0 s⁻¹ per Pd), as predicted by our conclusion. We note that in Figure 2c, 400 °C He treatment (blue) has no effects on the rWGS rate, eliminating the possibility that the activation is caused by the de-hydroxylation of TiO₂ surfaces. Since the effects of the rWGS stream on the structure and activity of Pd is a combination of the effects of H₂ and CO, we will mostly focus on the characterization of fresh, H400, and CO400 Pd₁/TiO₂, to understand the physical origins of these observations.

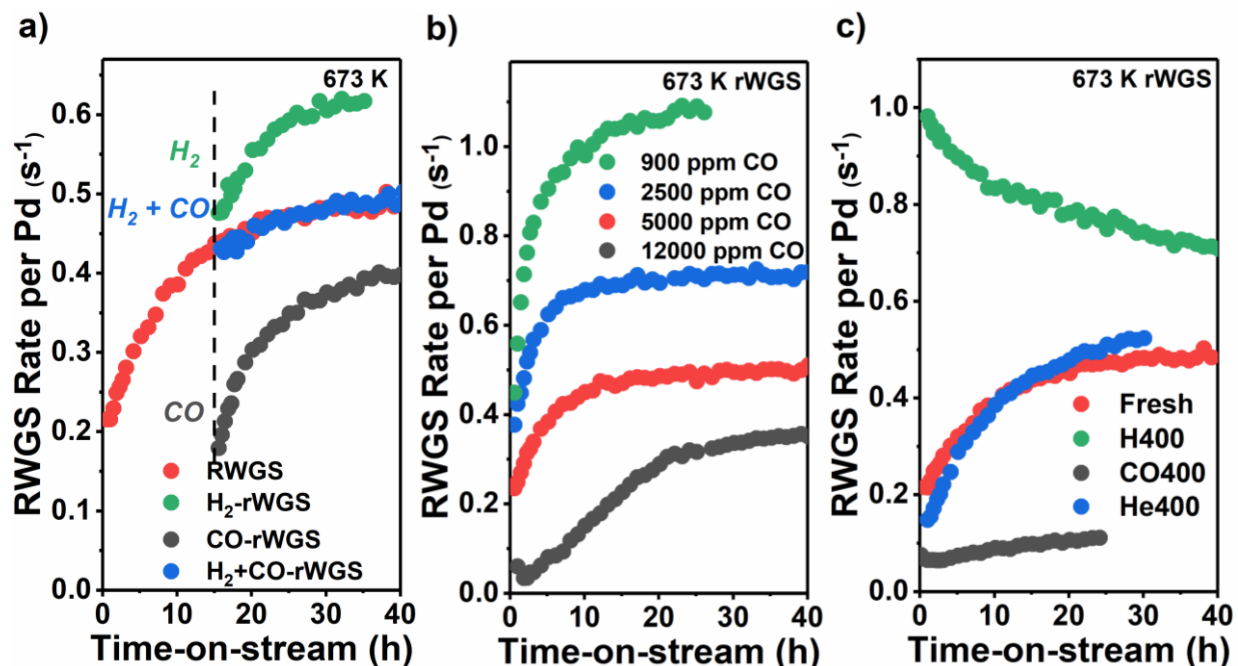


Figure 2. Variations in the rWGS rate per Pd with TOS at 400 °C on 0.0125 wt% Pd₁/TiO₂ showing the effects of H₂ and CO: **a)** Pd₁/TiO₂ in the first 15 h under the rWGS stream (red, 40% H₂, 10% CO₂, ~5% CO₂ conversion), 40% H₂ (green), 5000 ppm CO (black), and 40% H₂ + 5000 ppm CO (blue) at 400 °C; **b)** with various CO concentrations in the rWGS stream: 900 (green, 5 mg catalyst), 2500 (blue, 20 mg catalyst), 5000 (red), and 12000 ppm (CO, 10000 ppm CO added); **c)** after pre-treating Pd₁/TiO₂ with no treatment (red), 40% H₂ at 400 °C for 40 h (green), 5% CO at 400 °C for 24 h (black), and He at 400 °C for 24 h (blue). Typical reaction conditions are identical with Figure 1.

2. Dynamic coordination environment and metal nuclearity in Pd₁/TiO₂ under H₂ and CO

The nuclearity of Pd was evaluated by STEM, with results summarized in Figure 3. The fresh catalyst has exclusively Pd₁ (Figure 3a) with no signs of Pd aggregates. The atomic dispersion of Pd is supported by CO-IR, which only shows the 2112 cm⁻¹ band from CO linearly adsorbed on cationic Pd (Figure S1, fwhm ≈ 20 cm⁻¹, suggesting non-uniform environments of Pd₁),^{27,56-59} with no bridging CO on adjacent Pd sites (1800 ~ 2000 cm⁻¹). On the H400 catalyst, both Pd₁ (Figure 3b) and Pd aggregates of $d = 1.2 \pm 0.3$ nm (Figure 3c) were identified, indicating that a fraction of Pd₁ sinter into small Pd clusters (“Pd_n”) under H₂. These Pd_n do not exhibit well-defined three-

dimensional structure, and instead, are flattened plates, suggested by their low contrast with TiO_2 , and appear to be disordered. Meanwhile, CO adsorption on H400 Pd_1/TiO_2 yields a broad IR band between 2100 and 2040 cm^{-1} from linear CO on various surface sites on Pd aggregates (Figure S1),⁵⁶⁻⁵⁹ along with the 2114 cm^{-1} linear CO on $\text{Pd}^{\text{m}+}$ peak, supporting the partial sintering of Pd_1 into Pd_n . In contrast, on the CO400 catalyst, only large Pd nanoparticles of $d = 5.0 \pm 0.7$ nm (“ Pd_{NP} ”) were identified, with no Pd_1 , suggesting complete, severe Pd_1 sintering under CO. These Pd_{NP} have very bright contrast compared to TiO_2 , and Pd lattice diffraction can be observed (Figure S6d), indicating that unlike Pd_n , they are three-dimensional and crystalline.

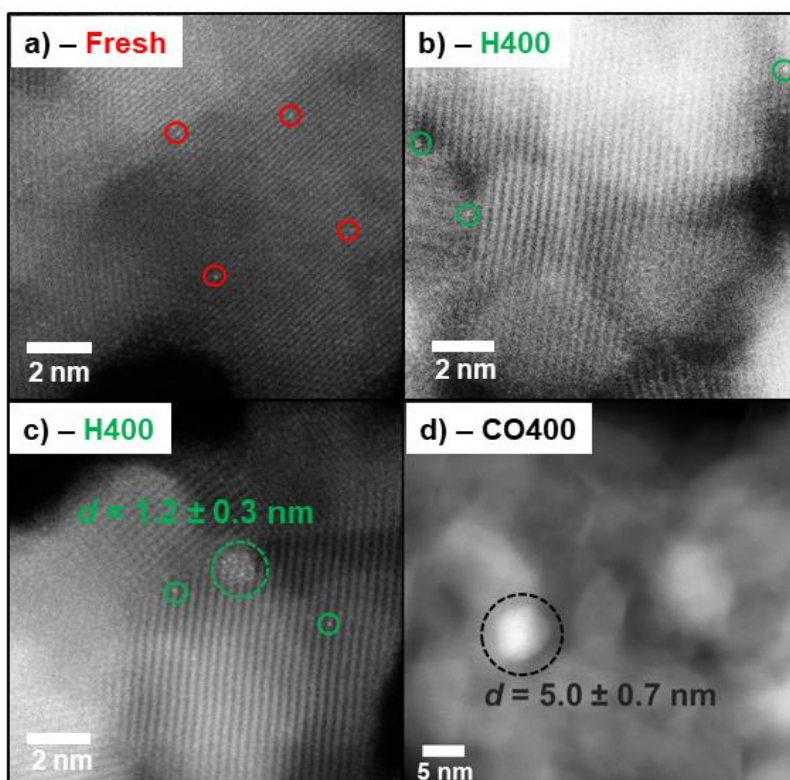


Figure 3. HAADF-STEM images of 0.0125 wt% Pd_1/TiO_2 : **a)** a representative image of the fresh sample, with only Pd_1 (in red circle) found; **b)** and **c)** two types of representative images of the H400 sample (transferred immediately into the vacuum after the treatment), one with only Pd_1 (in green circle), one with Pd_n of $d = 1.2 \pm 0.3$ nm (in green dashed circle) found; **d)** a representative image of the CO400 sample, with only Pd_{NP} of $d = 5.0 \pm 0.7$ nm (in black dashed circles) found. Additional images are included in Figures S6-7 to show the representativeness of the images and the lack of electron-beam artifacts.

The local coordination environment and oxidation state of Pd sites were examined by *in-situ* Pd K-edge XAS, with results summarized in Figure 4 and Table 1. For fresh Pd₁/TiO₂, the best model to fit its EXAFS between 1 and 4 Å includes a Pd–O single scattering path at 2.00 Å, a bonding distance, a Pd–Ti single scattering path at 2.95 Å, a non-bonding next-neighbor interaction, and a Pd–O single scattering path at 3.87 Å, a next-next-neighbor interaction (red in Figure 4a, Table 1). Replacing the Pd–Ti path with a Pd–Pd path led to poor agreement with the data between 2 and 3 Å (Figure S8a). Therefore, we deduce that the EXAFS of fresh Pd₁/TiO₂ has negligible contribution from Pd–Pd, further confirming that the Pd is predominantly atomically dispersed, and the average coordination number (*N*) of Pd₁ with the nearest O (*R* ≈ 2.00 Å) is 3.2 ± 0.4 (Table 1). In the XANES region (Figure 4b), the white-line intensity, the energy at which the edge starts to rise (edge onset energy), and the edge line shape of fresh Pd₁/TiO₂ (red) are all similar with those of PdO (cyan), indicating that the oxidation state of fresh Pd₁ is close to Pd(II).

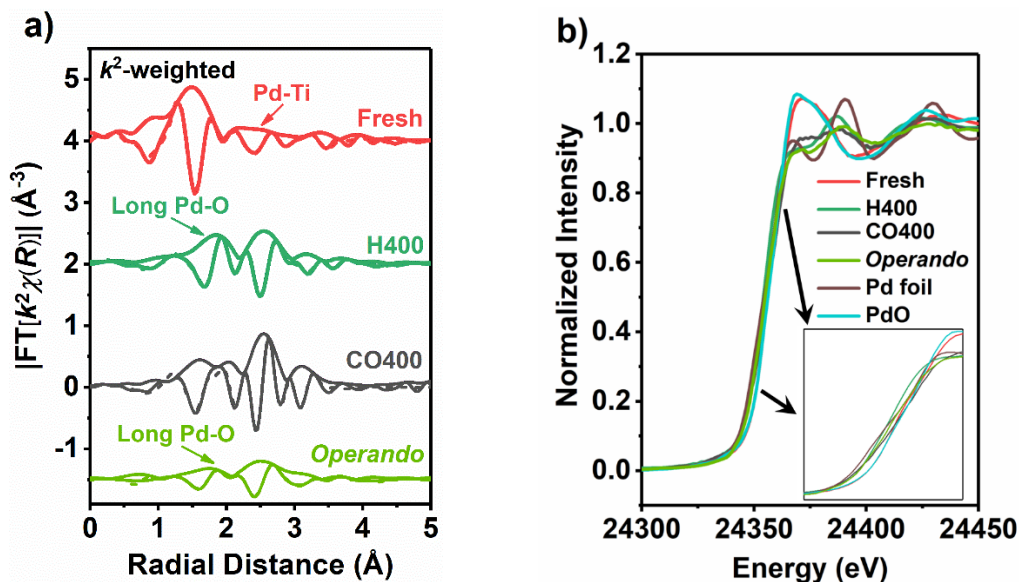


Figure 4. Pd K-edge XAS results on 0.0125 wt% Pd₁/TiO₂: **a)** EXAFS (*R*-space magnitude and imaginary part, best fitting shown as dashed curves, raw χ data shown in Figure S8c); **b)** XANES (the inset magnifying the edge). Red, green, and black curves represent the fresh, H400 (collected *in-situ*), CO400 (collected *ex-situ* after air exposure) catalysts respectively. The light green curves represent data collected *operando* at steady state (450 °C, 5% H₂). Brown and cyan curves represent Pd foil and PdO standards. The EXAFS fitting parameters are listed in Table 1.

Table 1. Fitting parameters from the best EXAFS models of 0.0125 wt% Pd₁/TiO₂

Catalyst status		Fresh	H400	CO400 (<i>ex-situ</i>)	<i>Operando</i>
k range (Å ⁻¹)				3 to 9.6	
R range (Å)				1 to 4	
S_o^2			0.82		0.75
ΔE_o (eV)		1 (1)	-7.2 (6)	3 (1)	-4 (1)
Pd-O (bonding, normal)	N	3.2 (4)	0.4	1.1 (6)	0.9 (5)
	R (Å)	2.00 (1)	2.13 (4)	1.99 (3)	2.08 (4)
	σ^2	0.003 (1)	0.005	0.004 (2)	0.013
Pd-O (bonding, long)	N		2.7 (3)		2.0 (9)
	R (Å)	N/A	2.533 (7)	N/A	2.41 (3)
	σ^2		0.005		0.013
Pd-Pd (metallic, bonding)	N		6.8 (6)	5 (1)	8 (2)
	R (Å)	N/A	2.761 (6)	2.75 (2)	2.72 (2)
	σ^2		0.015 (1)	0.009 (3)	0.023 (3)
Pd-Ti (non-bonding)	N	1.2 (3)			
	R (Å)	2.95 (3)	N/A	N/A	N/A
	σ^2	0.007			
Pd-Pd (oxide)	N			0.7 (5)	
	R (Å)	N/A	N/A	3.02 (7)	N/A
	σ^2			0.004	
Pd-Pd (oxide)	N			1.4 (7)	
	R (Å)	N/A	N/A	3.41 (3)	N/A
	σ^2			0.004	
Pd-O (next-next- neighbor)	N	7 (2)			
	R (Å)	3.87 (3)	N/A	N/A	N/A
	σ^2	0.012			
Pd-Pd (metallic, next-next- neighbor)	N		1.6 (4)		1.2 (7)
	R (Å)	N/A	3.83 (2)	N/A	3.75 (4)
	σ^2		0.008		0.012

Numbers in brackets are fitting standard deviations of the last digit. S_o^2 was determined by fitting the EXAFS of Pd foil. Two paths were used to represent Pd-Pd scattering in the oxide form based on the structure of PdO. *Operando* data were collected at 450 °C while others were collected at room temperature at a different beamline, leading to different σ^2 and S_o^2 values. H₂ treatment was performed at 450 °C to expedite the experiment.

After activation with H₂, a Pd–Pd scattering path appears in the EXAFS (green in Figure 4a, ~ 2.4 Å in the k^2 -weighted plot), consistent with the formation of Pd_n. The mean square deviation in half-path length of the Pd–Pd path ($\sigma^2 = 0.015 \pm 0.001$) is much higher than normal values for crystalline Pd at the same temperature (e.g., 0.005 ± 0.001 for Pd foil, Table S2), implying high disorder in the Pd–Pd bonds, echoing with Pd_n appearing disordered in STEM. If Pd_n were of hemi-spherical shape, the $N(\text{Pd–Pd}_1)$, i.e., the coordination number of directly bonded Pd–Pd, value of 6.8 ± 0.6 on H400 Pd₁/TiO₂ (Table S2) would predict $N(\text{Pd–Pd}_2) \approx 3.2$.⁶⁰ The actual $N(\text{Pd–Pd}_2) = 1.6 \pm 0.4$ (Table 1) is lower than the predicted value assuming hemi-spherical shape, indicating that Pd_n are flattened, consistent with the low contrast in STEM (Figure 3c). Interestingly, Table 1). Such long M–O bonds on H₂-reduced metal-oxide catalysts have been previously reported,^{61–67} and suggest that the Pd/TiO₂ interface is partially cleaved by H₂-reduction. Such cleavage could be a result of the hydroxylation of the interface, as previous works and theoretical calculation suggested.^{39, 62, 68, 69} We note that the EXAFS oscillations resulting from the long Pd–O path cannot be from Pd–Ti scattering, as its imaginary part is out of phase with Pd–Ti (Figure S8b), and thus cannot be properly fit with a model replacing the long Pd–O path with a Pd–Ti path. Meanwhile, in the XANES region (Figure 4b), the white-line intensity of H400 Pd₁/TiO₂ (green) is slightly lower than that of Pd foil (brown), and both the edge onset energy and the edge line shape are obviously different (inset showing the zoom-in view of the edge), suggesting that the electronic structure of Pd sites on H400 Pd₁/TiO₂ is different from that of regular metallic Pd.

The EXAFS of CO400 Pd₁/TiO₂ is dominated by Pd–Pd scattering between 2.4 and 3.5 Å (black in Figure 4a). Even though, this sample was measured after air exposure, most of the Pd appears to be metallic (Pd–Pd scattering path at $R = 2.75 \pm 0.02$ Å, Table 1), and in the XANES

region (Figure 4b), both the white-line intensity and the edge line shape resemble those of Pd foil (black compared to brown). Besides, $\sigma^2(\text{Pd-Pd})$ values (0.009 ± 0.003 and 0.004 for metallic and oxide paths) are normal for crystalline Pd. These characteristics suggest that after the CO treatment, most Pd₁ agglomerate into crystalline, metallic Pd_{NP} stable under room-temperature air, consistent with the STEM images showing three-dimensional crystalline Pd_{NP}. In summary, the combination of STEM, XAS, and CO-IR revealed that under H₂, some Pd₁ form small, disordered, flattened Pd_n plates, while under CO, all Pd₁ form large, crystalline, three-dimensional Pd_{NP}. Also, the H₂-reduction of Pd₁/TiO₂ creates elongated Pd-O bonds, i.e., partially cleaved MSI, and Pd sites with distinct electronic structures from metallic Pd.

XAS was also collected *operando* when the reaction starting from fresh Pd₁/TiO₂ reaches the steady state, i.e., rate plateau. The EXAFS (light green in Figure 4a) shows that most Pd-O bonds are elongated to $R = 2.41 \pm 0.03 \text{ \AA}$ (Table 1), and small, flattened, and disordered Pd_n ($N(\text{Pd-Pd}_1) = 8 \pm 2$, corresponding with $d \sim 1.5 \text{ nm}$; $N(\text{Pd-Pd}_2) = 1.2 \pm 0.7$, compared to the predicted value from hemisphere shape 4, $\sigma^2 = 0.023 \pm 0.003$) are formed. Meanwhile, the XANES (light green in Figure 4b) shows significantly different electronic structure of Pd from metallic, with slightly lower white-line intensity. All XAS characteristics at the steady state resemble those of H400 Pd₁/TiO₂, suggesting that active Pd sites formed on Pd₁/TiO₂ in *operando* conditions are similar with the highly active ones formed under H₂, as implied by Figure 2. In the *operando*-treated catalyst, the length of the Pd-O bond is slightly shorter and the fraction of them in all Pd-O is lower (69% compared to 90%) than those on H400 Pd₁/TiO₂ due to lower H₂ concentration used (5% compared to 20%), while the slightly larger Pd_n size could reflect the effect of trace (~ 1000 ppm) CO.

The effects of H₂ and CO treatments on the structure of Pd/TiO₂ were further examined by atomistic simulations. First, we performed *ab initio* molecular dynamics (AIMD) simulations of a Pd₁₃ cluster on anatase TiO₂(101) (Pd₁₃/TiO₂) in the presence of H atoms and CO molecules, separately, to compare the morphology of Pd aggregates formed under H₂ and CO. At the start of the simulation, 32 H atoms or 16 CO molecules were placed randomly on the TiO₂ surface and on the Pd₁₃ aggregate. During the simulation, 5 H₂ molecules and 4 CO molecules desorbed, respectively. Pd₁₃/TiO₂ without adsorbates was also simulated for comparison. The final equilibrated geometries of all simulated systems are shown in Figure 5a. To quantify the dimensionality of the Pd₁₃ cluster over time, we tracked the *z* coordinate of the Pd atoms relative to the cluster's center of mass via the following equation:

$$R_z(t) = \sqrt{\frac{\sum_{i=1}^{N_{Pd}} (r_z^i(t) - \bar{R}_z(t))^2}{N_{Pd}}},$$

where $r_z^i(t)$ is the *z* coordinate of the *i*th Pd atom at time *t*, $\bar{R}_z(t)$ is the center of mass of all Pd atoms at time *t*, and N_{Pd} is the number of Pd atoms (13). $R_z(t)$ was plotted for all three systems in Figure 5b. We observe that the Pd₁₃ center of mass distribution in the CO-Pd₁₃/TiO₂ system is consistently higher than that in the Pd₁₃/TiO₂ and H-Pd₁₃/TiO₂ systems, indicating that in the presence of CO, the Pd atoms, on average, are more likely to be found farther away from the TiO₂ surface than they are in the presence of H or for the neat system. We also plotted the density of Pd atoms as a function of distance from the TiO₂ surface in Figure 5c, where the density was taken over the entire AIMD trajectories. In this case, we observe similar atomic density distributions for the Pd₁₃/TiO₂ and H-Pd₁₃/TiO₂ systems with two major peaks, which indicate that the Pd₁₃ cluster is mostly organized in two layers. In the case of CO-Pd₁₃/TiO₂, however, we observe three peaks indicative of an emerging third layer and thus, overall, a more three-dimensional structure of the

Pd₁₃ cluster. The AIMD results are consistent with the experimental observations of flattened Pd plates on H400 and three-dimensional Pd particles on CO400 Pd₁/TiO₂.

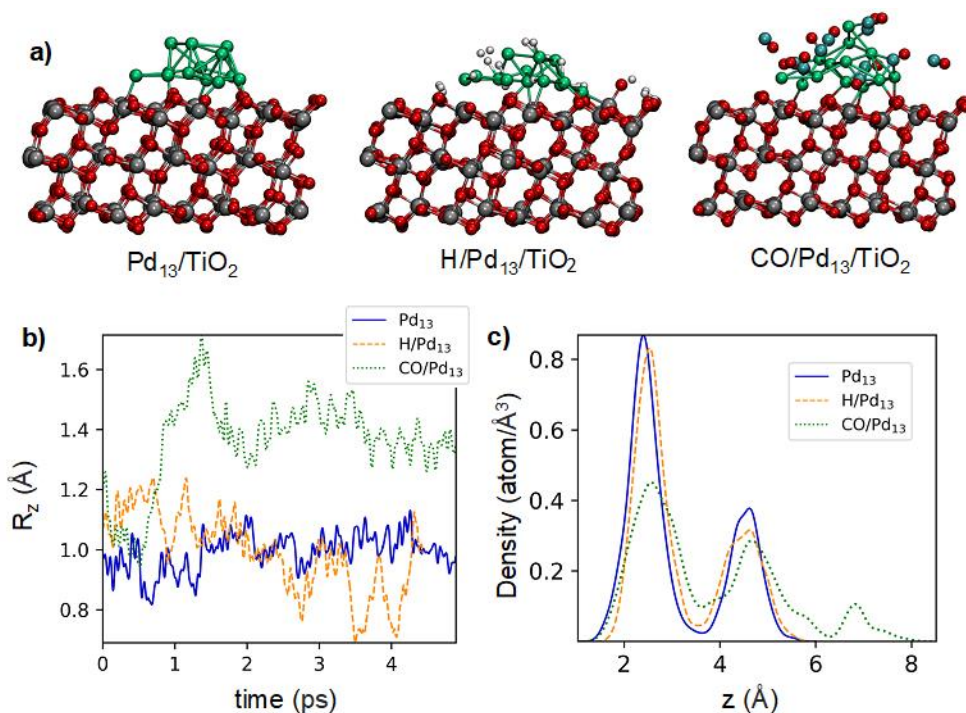


Figure 5. **a)** Final geometries of the three simulated systems (color codes: O in red, Ti in grey, Pd in lime, C in cyan, H in dark white); **b)** $R_z(t)$ for Pd₁₃/TiO₂, H-Pd₁₃/TiO₂, and CO-Pd₁₃/TiO₂; **c)** Pd density as a function of distance from the TiO₂ surface.

Meanwhile, to examine the changes in the coordination environment of Pd on Pd₁/TiO₂ under H₂, we performed density functional theory (DFT) calculations on Pd₁/TiO₂ with and without adsorbed H atoms. In agreement with Jin *et al.*,⁷⁰ our calculations show that without adsorbates, the most stable adsorption site for Pd₁ on the anatase TiO₂(101) surface is the OO site, where the Pd atom bridges two two-fold coordinated oxygen atoms (O_{2C}), as shown in Figure 6a, with the average Pd–O bond length $r_{\text{Pd-O}}$ of 2.1 Å for the nearest O neighbors. The calculated $r_{\text{Pd-O}}$ matches the $R(\text{Pd-O}_1)$ on fresh Pd₁/TiO₂ from the EXAFS fitting (Table 1), while the apparent difference in the nearest Pd–O coordination number is likely due to O₂ adsorption on the sample.

Several different adsorption sites for CO and H₂ on Pd₁/TiO₂ were tested and the most stable configurations for H₂-Pd₁/TiO₂ and CO-Pd₁/TiO₂ are shown in Figures 6b and 6c respectively. Upon the adsorption of H₂, Pd₁ moves from the OO site to a neighboring OTi site. The average $r_{\text{Pd-O}}$ were computed, together with the Bader charge on Pd, q_{Pd} , for Pd₁/TiO₂ and all H₂-Pd₁/TiO₂ and CO-Pd₁/TiO₂ configurations. Below each structure in Figure 6, we show q_{Pd} and $r_{\text{Pd-O}}$, for the most stable configurations (complete results are shown in Figure S11a). It is clear that H₂ adsorption significantly increases $r_{\text{Pd-O}}$ from 2.1 Å to 2.5 Å and decreases q_{Pd} , i.e., increases the electron density on Pd₁. Therefore, the results of DFT calculations confirm the conclusions of the EXAFS analysis, i.e., H₂ treatment changes the coordination environment of Pd in a way that elongates the Pd–O interfacial bonds to ~2.5 Å, and modifies the electronic structure of Pd, while CO treatment has no such effects.

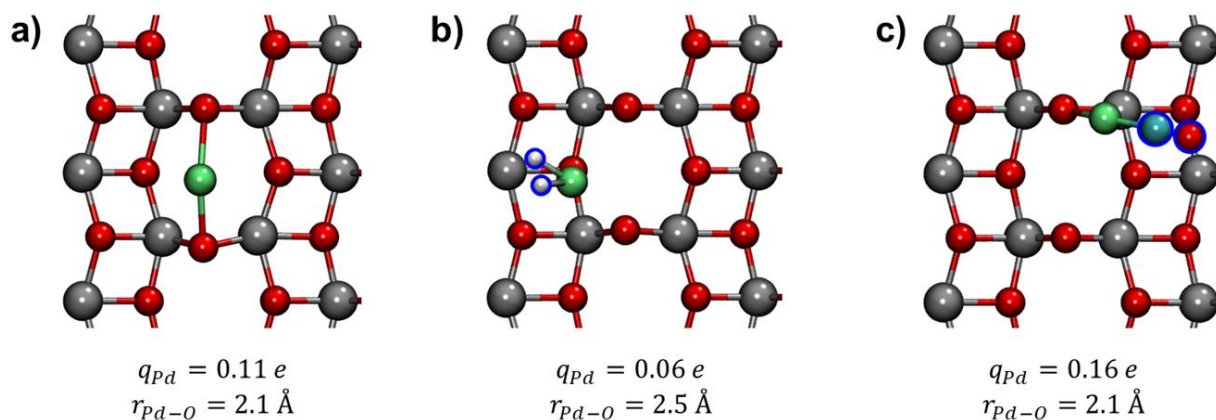


Figure 6. Top view of the optimized geometries and corresponding Bader charges q_{Pd} of Pd₁ and Pd–O bond length $r_{\text{Pd-O}}$ of **a)** Pd₁/TiO₂(101), **b)** H₂-Pd₁/TiO₂(101), and **c)** CO-Pd₁/TiO₂(101). Color codes: O in red, Ti in gray, Pd in lime, C in cyan, and H in dark white. Adsorbate atoms (CO and H) are highlighted in blue.

3. *H₂-induced high intrinsic activity of Pd due to changes in coordination environment*

Characterization results above offer a clear, logical explanation to the deactivation by CO: the severe sintering of Pd₁ decreases the number of active sites. Nonetheless, the origin of the activation by H₂ remains unsettled, as under H₂, both the nuclearity (minor sintering) and coordination environment (partial MSI cleavage and electronic structure modification) of Pd change. The effects of the two were deconvoluted by analyzing a H400 Pd₁/TiO₂ sample exposed to room-temperature air for two months (“H400_ART”). STEM shows that H400_ART Pd₁/TiO₂ has similar nuclearity with H400 Pd₁/TiO₂, i.e., a mixture of Pd₁ (Figure 7a) and small Pd clusters (Figure 7b) of $d = 1.1 \pm 0.2$ nm (close to $d = 1.2 \pm 0.3$ nm in Figure 3c). The similar nuclearity on the two samples is further supported by the similar $N(\text{Pd-Pd}_1)$ in the EXAFS: 6.8 ± 0.6 (Table 1) compared to 7 ± 1 (Table S2). Meanwhile, the EXAFS also suggests that the direct Pd–O bonds on H400_ART Pd₁/TiO₂ (purple in Figure 7d) are of normal length ($R = 1.99 \pm 0.01$ Å, Table S2), instead of the elongated $R = 2.533 \pm 0.007$ Å on H400 Pd₁/TiO₂. In the XANES region (Figure 7e), both the white-line intensity and the edge onset energy of H400_ART Pd₁/TiO₂ (purple) resemble those of PdO (cyan), rather than Pd foil (brown), suggesting Pd²⁺ sites, instead of the electron-rich Pd sites on H400 Pd₁/TiO₂. Therefore, we conclude that the room-temperature oxidation reverses the changes in Pd coordination environment under H₂ but does not reverse the changes in Pd nuclearity.

In the rWGS (Figure 7f), H400_ART Pd₁/TiO₂ (purple) exhibits identical behaviors with the fresh (red) catalyst, in contrast to the H400 catalyst that shows high, but decreasing rate (green in Figure 1c). This directly proves that the H₂-induced high intrinsic activity is due to the changes in Pd coordination environment, i.e., partial MSI cleavage and the unique electronic structure, instead of the formation of Pd_n. This conclusion is further supported by the following observations.

First, the activation by H₂ requires > 15 h at ≥ 350 °C while the sintering occurs at 200 °C in 3 h (Figure 1b). In fact, *operando* XAS during the induction period on fresh Pd₁/TiO₂ indicates similar level of sintering ($N(\text{Pd-Pd}_1) = 8 \pm 4$, Table S2) compared to the steady state, but incomplete MSI cleavage of 41% compared to 69% of elongated Pd–O bonds and electronic state modification (XANES in Figure S9b). Second, the final rate on Pd₁/TiO₂ increases monotonically when Pd₁ coverage decreases (Figure 1a). Third, treating Pd₁/TiO₂ at steady state with He leads to a decrease in rate, which is recovered quickly by re-initiating the rWGS (Figure S12a). Meanwhile, XAS suggests that the He treatment does not disintegrate Pd_n (Table S2), but increases the white-line intensity to a level close to metallic Pd (Figure S12b). The change in Pd electronic state under He is reversed by re-initiating the rWGS (Figure S12b), consistent with the observed rate change. It is likely caused by the desorption of *H.

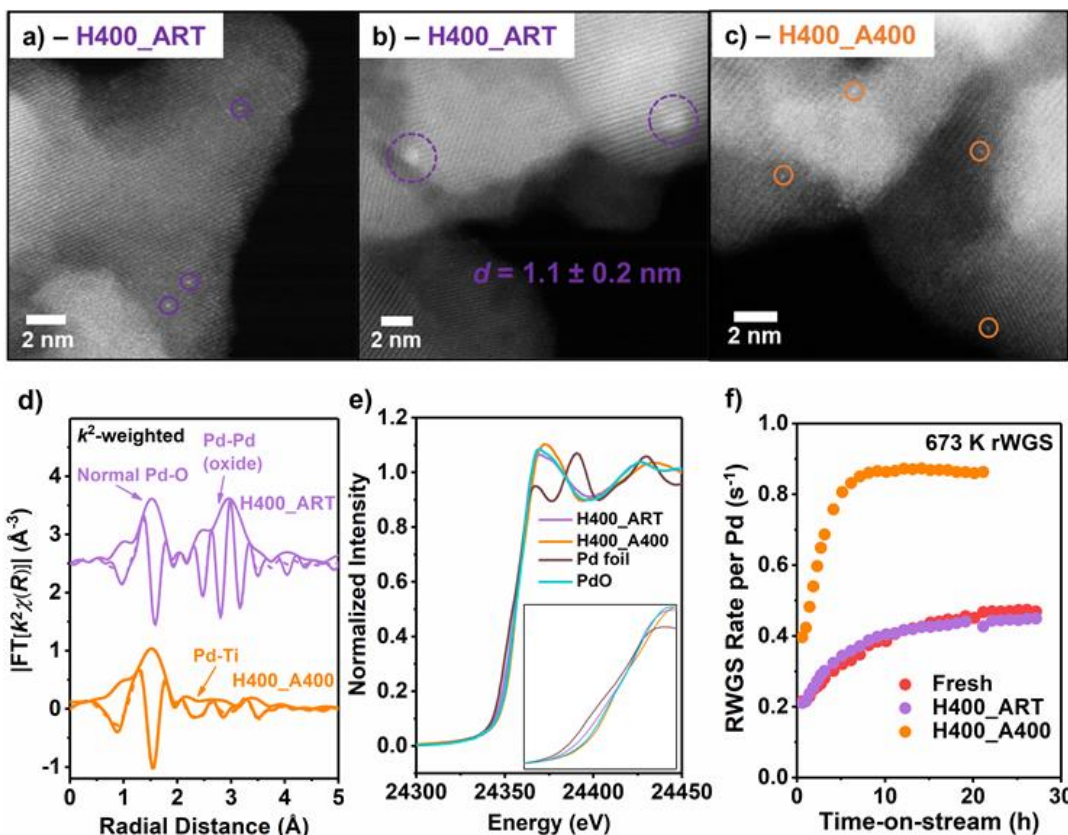


Figure 7. Characterization and kinetic results on H400 Pd₁/TiO₂ oxidized at room temperature (purple, H400_ART) and 400 °C (orange, H400_A400): **a)** and **b)** two types of representative images of the H400_ART sample, one with only Pd₁, one with Pd clusters of $d = 1.2 \pm 0.3$ nm found; **c)** a representative image of the H400_A400 sample, with only Pd₁ found; **d)** and **e)** EXAFS (R -space magnitude and imaginary part, best fitting shown as dashed curves, raw χ data shown in Figure S8c) and XANES (the inset magnifying the edge) of the two samples, respectively. The EXAFS fitting parameters are listed in Table S2. Brown and cyan curves in panel **e)** represent Pd foil and PdO standard as references. The oxidation in XAS measurements was performed with 20% O₂ in He instead of air; **f)** variations in the rWGS rate per Pd with TOS under identical conditions with Figure 1.

4. High-temperature oxidation re-disperses Pd_n, facilitating the rWGS and TiO₂ reduction

We previously reported that small, flat, and disordered Pt_n can be re-dispersed into Pt₁ by oxidation at room temperature,³⁷ but Figure 7 shows that Pd_n, despite having similar structure with Pt_n, are only oxidized but not re-dispersed. Therefore, we attempted to re-disperse Pd_n on H400 Pd₁/TiO₂ by oxidation at 400 °C in air (“H400_A400”). Figure 7 shows that H400_A400 Pd₁/TiO₂ only has Pd₁ in STEM (Figure 7c), and its EXAFS (orange in Figure 7d, Table S2) resembles that

of fresh Pd₁/TiO₂: it has no Pd–Pd scattering, is best modelled by two Pd–O (directly bounded and next-next-neighbor) and one Pd–Ti paths (Figure S8a), with similar $N(\text{Pd–O}_1)$ (4.0 ± 0.5 compared to 3.2 ± 0.4). In XANES (Figure 7e), the white-line intensity, edge onset energy, and edge line shape of H400_A400 Pd₁/TiO₂ (orange) are all close to that of PdO (cyan) and fresh Pd₁/TiO₂. Therefore, all Pd on H400_A400 Pd₁/TiO₂ exist as Pd₁ in similar coordination environment with Pd₁ on fresh Pd₁/TiO₂, i.e., Pd_n can be re-dispersed into Pd₁ by high-temperature oxidation.

Surprisingly, H400_A400 Pd₁/TiO₂ shows higher rWGS rate and faster rate increase with TOS (orange in Figure 7f) than fresh Pd₁/TiO₂ (red), despite having spectroscopically similar Pd₁ sites with the latter. Directly oxidizing fresh Pd₁/TiO₂ at 400 °C (“A400”) also has the promotion effects but treating it with 400 °C He does not (Figure S13), suggesting that the promotion is not due to pure thermal effects, such as TiO₂ de-hydroxylation. After the activation by H₂, the two samples also have Pd species of similar nuclearity and coordination environment (suggested by the highly similar EXAFS, “H400_A400_H400” and H400 in Figure S8b, Table S2, and Table 1). Thus, the superior activity of H400_A400 Pd₁/TiO₂ cannot be attributed to different Pd nuclearity or MSI structure. The difference between the two was revealed by IR: the triplet $\nu(\text{CH})$ bands at 2963, 2928, and 2854 cm⁻¹ on fresh Pd₁/TiO₂ disappear after 400 °C oxidation (Figure S14a). These bands are from mixed carboxylate layers adsorbed on TiO₂⁷¹⁻⁷⁵ from ppm-level carboxylic acids in air,⁷⁶⁻⁷⁸ which is supported by XPS (Figure S14b). We have previously shown that adsorbed carboxylate layers are detrimental to the rWGS catalysis,⁷⁹ and thus their removal explains the higher rWGS rate. This is supported by the results in Figure S13b: the promotion effect of the A400 treatment on Pd₁/TiO₂ decays gradually with subsequent room-temperature air exposure, during which the carboxylate layers would re-accumulate. We note that the A400 treatment also promotes the rWGS activity of pristine TiO₂, which decays with room-temperature

air exposure as well (Figure S15), further supporting that the effects are due to changes on TiO₂, and not of Pd.

Meanwhile, the rate increase with TOS is faster and more significant on H400_A400 than over fresh Pd₁/TiO₂. Since the rate increase is due to changes in the Pd coordination environment caused by catalyst reduction, the observation infers that H400_A400 Pd₁/TiO₂ is easier to reduce than fresh Pd₁/TiO₂. For confirmation, we tracked the evolution of IR spectra of the two samples under H₂ at 400 °C, in which bulk TiO₂ reduction leads to increased absorbance between 2000 and 1200 cm⁻¹ as electrons are injected into the conduction band edge (CBE) of TiO₂.⁸⁰⁻⁸² Figures 8a and 8b show series of IR spectra collected from the fresh and H400_A400 Pd₁/TiO₂, respectively, and the changes in the IR absorbance (ΔA) in the CBE region (represented by 1740 cm⁻¹) relative to $t = 0$ h with reduction time are shown in Figure 8c. ΔA increases more than 10 times faster on H400_A400 (orange in Figure 8c) than fresh Pd₁/TiO₂ (red), confirming the much more facile TiO₂ reduction on the former. This is likely due to the removal of the carboxylate layers reducing barriers for O_v/electron migration. The faster, deeper bulk TiO₂ reduction (Figure 8c) coincides with the faster, more significant intrinsic activity increase of Pd (Figure 7f), and the time scale of the two processes aligns well (~22 h for bulk TiO₂ reduction, compared to ~25 h for the intrinsic activity increase), implying that the changes in Pd coordination environment under H₂ are likely driven by the bulk reduction of the anatase support.

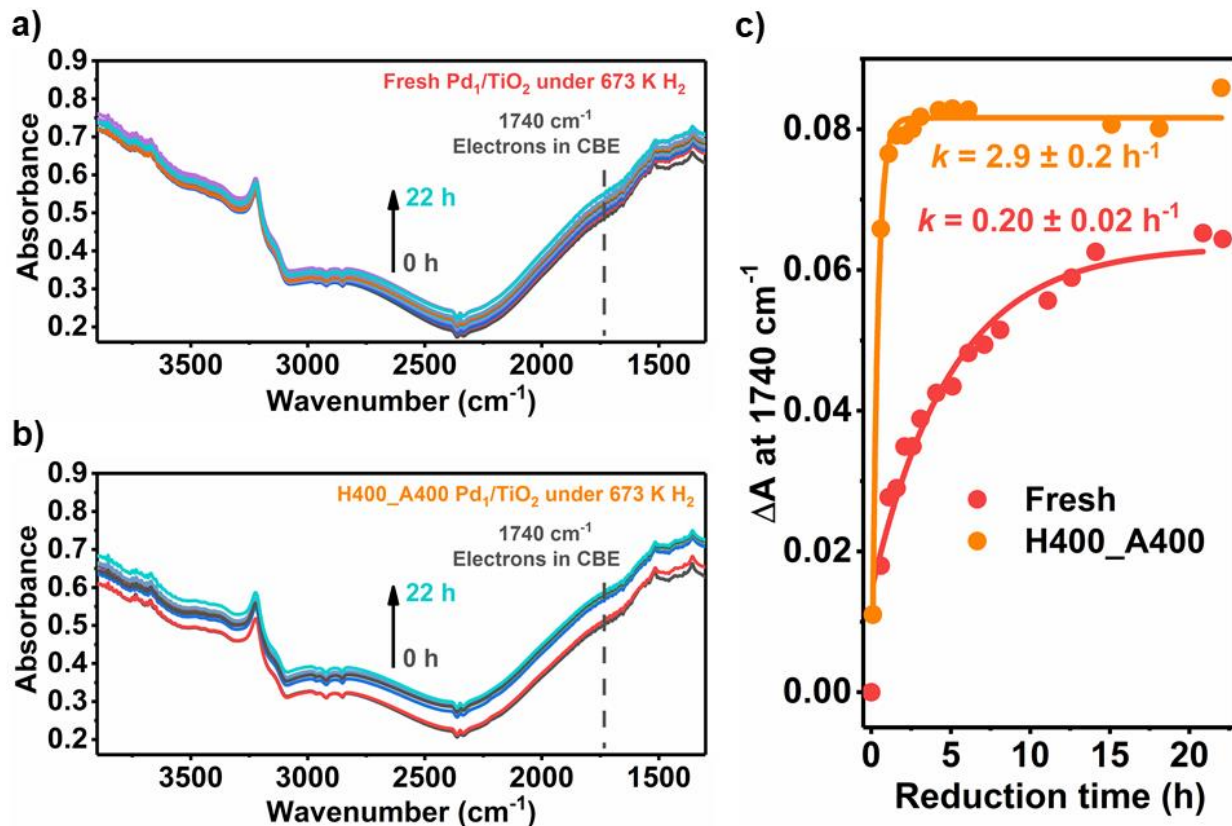


Figure 8. Evolution of IR spectra of 0.0125 wt% Pd₁/TiO₂ under 1 Torr H₂ at 400 °C: **a)** and **b)** fresh and H400_A400 (actual oxidation performed with 1 Torr O₂ in the vacuum chamber) samples respectively. Spectra from the bottom (black) to the top (cyan) were collected at $t = 0, 0.5, 1, 1.5, 2, 2.5, 3, 4, 5, 6, 8, 11, 12.5, 14, 20,$ and 22 h, respectively; **c)** variations in the relative absorbance (ΔA) at 1740 cm⁻¹ to $t = 0$, which reflects the amount of electrons injected into TiO₂, with the reduction time. The data were fit exponentially and k is the pseudo-first-order rate constant for the TiO₂ reduction.

5. H₂-modified Pd coordination environment mainly promotes the carboxyl rWGS pathway

We performed kinetic measurements on fresh and H400 Pd₁/TiO₂ at various temperatures to reveal mechanistic origins of the high intrinsic activity of Pd in the coordination environment modified by H₂. Figure 9a shows that both the rate enhancement (black) and the decrease in the apparent activation barrier ($E_{a,app}$, red and green for fresh and H400 Pd₁/TiO₂, respectively) after the activation by H₂ are more significant at higher temperature (no rate enhancement, similar $E_{a,app}$

at 200 °C; 3.6-fold rate increase, ~10 kJ/mol lower $E_{a,app}$ at 350 ~ 400 °C). We have previously shown that on supported noble metal catalysts, the rWGS proceeds through both the formate (*HCOO) pathway on large metal planes and the carboxyl (*COOH) pathway on peripheral MSI sites.^{39, 44, 79, 83-85} Between the two, the carboxyl pathway contributes more at higher temperature,³⁹ has lower $E_{a,app}$ (~46 compared to ~64 kJ/mol,⁷⁹ Table S3) and higher reaction order with respect to CO₂ (~0.61 compared to ~0.46,⁷⁹ Table S3). Figure 9b shows that as the reaction temperature increases from 200 to 400 °C, the CO₂ order on both fresh and H400 Pd₁/TiO₂ increases from ~0.45 to ~0.63, reflecting the mechanism shift from the formate to the carboxyl pathway. Therefore, the more significant activation effects by H₂ at higher temperature in Figure 9a indicates that the modification of Pd coordination environment mainly promotes the carboxyl pathway.

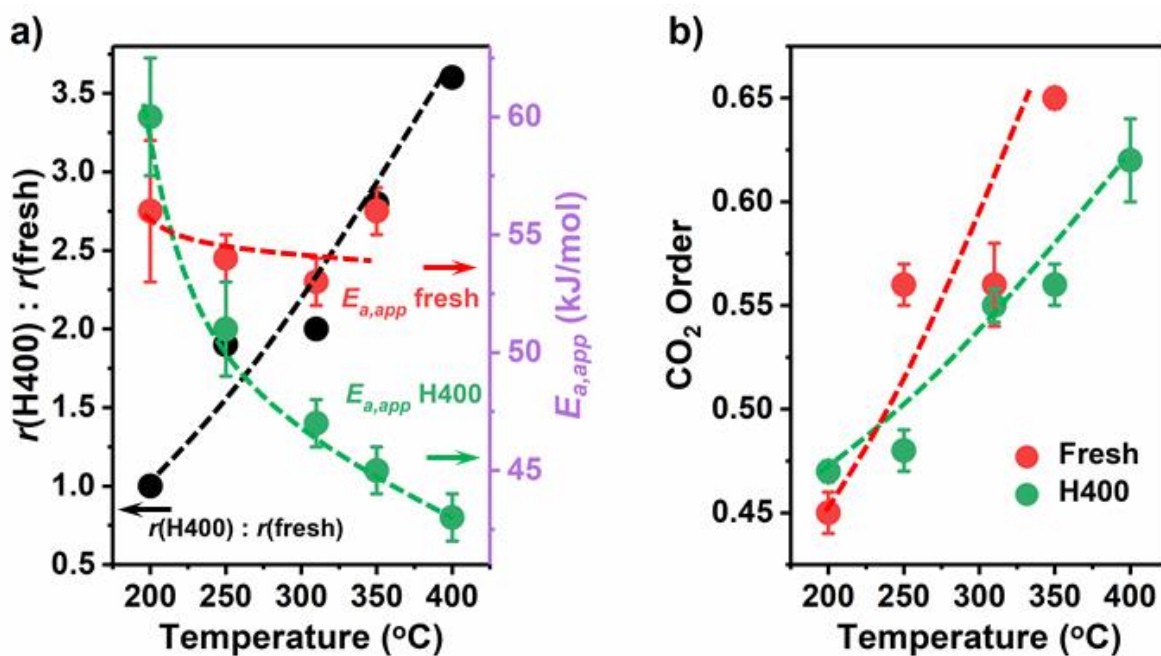


Figure 9. Measurements of the rWGS kinetics on fresh (red) and H400 (green) Pd₁/TiO₂: **a)** variations in the rate enhancement level (black dots/curve), i.e., the rate ratio between the H400 and fresh samples, and the apparent activation barrier ($E_{a,app}$) with the temperature; **b)** variations in the reaction order with respect to CO₂ with the temperature. Data cannot be obtained on fresh Pd₁/TiO₂ at 400 °C due to the fast activation. The reactions were performed with a total flow of 40 SCCM, H₂ concentration < 25%, CO₂ concentration < 10%, and CO₂ conversion < 5%.

This conclusion matches the prediction from our previous mechanistic studies, that the most active Pd sites for the carboxyl pathway are ones at the MSI with cleaved Pd–O interface with higher electron density than Pd(0), created *in-situ* by H₂ reduction.³⁹ The elongated Pd–O bonds and unique electronic structure of Pd on H400 Pd₁/TiO₂ (in particular the lower white-line intensity than metallic Pd) and the results obtained *operando* (Figure 4 and Table 1) align with the predicted active site structure, thus rationalizing the high intrinsic activity in the carboxyl pathway. The high intrinsic activity of such Pd sites was attributed to their better ability to 1) activate CO₂ and form the carboxyl intermediates, the rate-determining step of the carboxyl pathway³⁹ and 2) dissociate H₂ as the back donation to the H–H antibonding orbital is stronger with higher electron density.^{17, 86-88}

Discussion

1. Strong effects of the metal-support interaction on highly dispersed metal species

We have demonstrated that the reduction of TiO₂ by H₂ partially cleaves its interface with supported Pd₁/Pd_n, modifies their electronic structure, which enhances their intrinsic activity in the rWGS. This occurs despite, not because of, the partial sintering of Pd₁ to Pd_n. The significant IR absorbance increase in the CBE region (Figure 8) and the blue color of H400 Pd₁/TiO₂ suggest high reduction level of TiO₂. Nonetheless, no Ti³⁺ or O_v/OH were observed by the XPS (Figures S16a-c) in this catalyst, indicating that bulk O_v were formed rather than surface O_v/–OH, in agreement with the literature for TiO₂-A.⁵⁰⁻⁵³ Thus, the reduction of TiO₂-A alters the rWGS rate by changing the properties of Pd, instead of the reactivity of its surfaces. This is supported by Figure S15 showing that reducing TiO₂-A alone does not enhance its rWGS activity, and that the

formation of surface Ce^{3+} and $\text{O}_\text{v}/\text{OH}$ on H400 Pd/CeO₂ (Figures S16d-f) does not increase the rWGS rate. The lack of TiO₂ surface reduction on H400 Pd/TiO₂-A, along with the lack of Pd–Ti scattering in the EXAFS (Figures 4a and S8b), also eliminates the possibility of SMSI causing the high activity. Since the coordination environment of single metal atoms is solely defined by the support, changes in support properties, even in the bulk, could affect their reactivity significantly. In contrast, CO400 Pd₁/TiO₂ exhibits minimal rate increase with TOS (Figure 2c), indicating that bulk TiO₂ reduction has minimal effects on Pd_{NP}. This is because the coordination environment of Pd in Pd_{NP} is mostly determined by neighboring Pd, and thus less affected by the support. Also, on Pd_{NP}, a higher fraction of turnovers proceed through the formate pathway that is not affected by the MSI.³⁹ We note that recent studies show that the effects of support reduction depend on its size,⁸⁹ and that bulk ZnO reduction alters the electronic structure and reactivity of supported Au,⁹⁰⁻⁹³ in concert with this work.

With all metal sites at the MSI, SACs carry unique values in mechanistic studies, by enabling the direct observation of phenomena at the MSI that are difficult to probe on regular nanoparticle catalysts with ensemble-average characterization techniques. The most active Pd sites for the carboxyl rWGS pathway, the electron-rich MSI sites with partially cleaved Pd–O bonds, $\text{Pd}(\text{H})^{\delta-}\text{OH}$, were previously predicted by theory,³⁹ but not observed experimentally on nanoparticle catalysts. The XAS of H400 Pd₁/TiO₂ (Figure 4) provides experimental spectroscopic evidence for such sites. Although the minor sintering of Pd₁ reduces the fraction of MSI sites, the effect is alleviated by the flat shape of Pd_n. The MSI cleavage under H₂ was previously reported on metal-oxide catalysts in a limited number of studies.⁶¹⁻⁶⁷ Similar with this work, these studies also used catalysts with highly dispersed metal species ($d \leq 1$ nm). We note that the $\text{Pd}(\text{H})^{\delta-}\text{OH}$ active sites on Pd₁/TiO₂ are only preserved under H₂ or during the rWGS, and lost after being

exposed to room-temperature air (Figure 7), or He (Figure S12). This emphasizes the necessity of *in-situ/operando* spectroscopy in accurately understanding active sites on and dynamics of SACs.

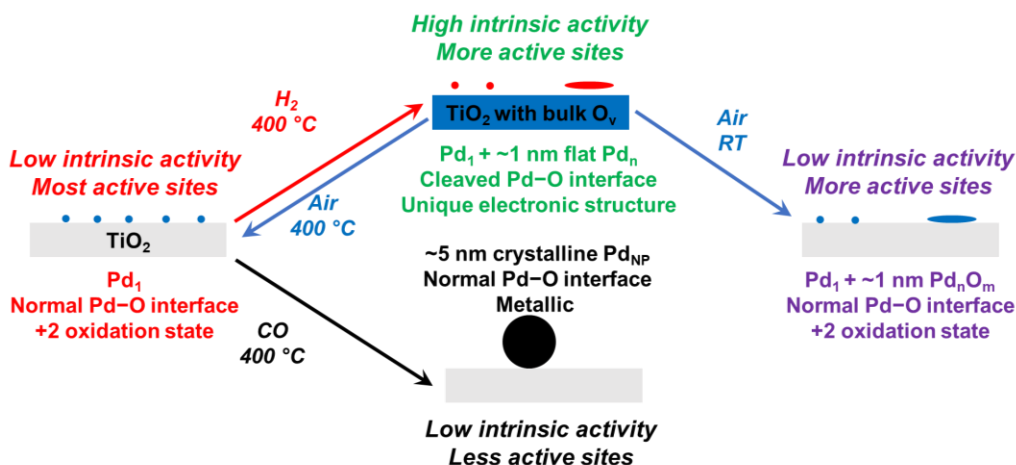
2. Dynamics of Pd₁/TiO₂-anatase and comparisons with similar systems

The structural evolution of Pd₁ on TiO₂-A is summarized in Scheme 1. The sintering of Pd₁ into ~5 nm crystalline Pd_{NP} under 400 °C CO is expected considering the high mobility of Pd(CO)_x, which aggregates even at room temperature.³⁵ In contrast, under H₂, only some Pd₁ sinter into ~1 nm disordered Pd_n. The contrast of Pd_n with TiO₂ in STEM images ranges from 2D-like to similar with regular particles, suggesting various thicknesses. In the EXAFS, completely 2D fcc metal clusters have no M–M₂ scattering ($R = 3.83 \text{ \AA}$ for Pd).⁹⁴⁻⁹⁶ Thus, the lower $N(\text{Pd-Pd}_2)$ of Pd_n than the expectation from hemi-spherical shape reflects the on-average flattened shape. We note that the total $N(\text{Pd-O}) = 3.1 \pm 0.3$ on H400 Pd₁/TiO₂ is high for Pd clusters of $d \approx 1.2 \text{ nm}$. This is due to both the presence of some Pd₁ (Figure 3b), and the fact that flattened plates have more Pd in contact with support oxygen than same-sized hemi-spherical particles.⁹⁴ The flattened, disordered, small M_n were reported to form under H₂ from other M₁ on reducible oxides as well,^{37, 96} and proposed to be stabilized by the electron transfer from the reduced support.^{37, 97-101} This hypothesis is supported by the fact that H400_A400_H400 Pd₁/TiO₂, which has more reduced TiO₂ (Figure 8c) than H400 Pd₁/TiO₂, have completely flat Pd_n, as suggested by $N(\text{Pd-Pd}_2) = 0$ (Table S2). Thus, when TiO₂ is oxidized by air, Pd_n become unstable. At room temperature, the barrier for the re-dispersion cannot be overcome, but Pd_n are oxidized (Figure 7 and Table S2) to Pd_n²⁺O_m, while under the same conditions, crystalline, three-dimensional Pd_{NP} mostly remain metallic (Figure 4 and Table 1). At 400 °C, they are completely re-dispersed into Pd₁ (Figure 7).

During the rWGS, the co-existence of H₂ and CO leads to a mixture of Pd₁, Pd_n and Pd_{NP}, as shown by STEM images of the post-reaction sample (Figure S17). This is further supported by

the observation that all XAS characteristics of Pd₁/TiO₂ used in the rWGS after room-temperature air exposure (“RWGS400_ART”) are between those of H400_ART and CO400_ART Pd₁/TiO₂ (Figure S18, Table S2). When the conversion and thus CO concentration is low, its effects on both rates (Figure 2b) and Pd structure (Figure 4) become negligible. At low Pd₁ coverage (≤ 0.025 wt%), sintering is minor. Thus, the higher intrinsic activity due to the activation by H₂ overcomes the decrease in dispersion, and the per-Pd reaction rate increases (Figure 1a). At high Pd₁ coverage (0.05 wt%), the two effects offset, leading to minimal rate changes with TOS. Since sintering is less demanding and faster than the activation by H₂, at ≤ 375 °C, the rate drop due to sintering can be captured initially (Figure 1b). Accounting for the sintering and assuming MSI active sites,^{39, 44} the 3.6-fold rate increase after the activation by H₂ corresponds with a ~4.5-fold increase in TOF.

The activation by H₂ of Pd₁/TiO₂ demands $T \geq 350$ °C (Figure 1b) and has a high activation barrier of ~120 kJ/mol (Figure S4), suggesting that it cannot be explained simply by Pd–H binding. This high barrier could be associated with O_v migration into anatase bulk (70 – 80 kJ/mol in the literature).^{51, 52, 102} Besides, as DFT suggests (Figure 6), Pd likely diffuses to other surface sites under H₂, which may also have high barriers (~100 kJ/mol in the literature for Pt₁ diffusion on anatase^{103, 104}). The process can be facilitated by higher H₂ pressure, as under high-pressure rWGS conditions (Figure S19, 21 bar H₂), the intrinsic activity increase can be observed at 300 °C, and on Pd_{NP}.



Scheme 1. Summary of the structural evolution of Pd₁/TiO₂ SAC under various atmospheres

Finally, we compare the dynamics of Pd₁/TiO₂ with systems we previously studied.^{27, 37} On TiO₂-A at 400 °C, Pt₁ also form stable, crystalline Pt_{NP} under CO, and ~1 nm, disordered, flat Pt_n under H₂. Nonetheless, the Pt–O interface remains intact under H₂, and thus the reduction does not increase rWGS rate.³⁷ The contrast between Pt and Pd again emphasizes that the rWGS activity of highly dispersed Pd/Pt is determined by their coordination environment, rather than nuclearity. The flat shape and small size (~1 nm) of Pt_n/Pd_n predict that ~80% Pt/Pd sites are at MSI, explaining the similar rWGS rate between fresh and H400_ART Pd₁/TiO₂ (Figure 7f). Pt and Pd also behave differently in the oxidative re-dispersion, which occurs at room temperature for Pt³⁷ but requires high temperature for Pd. Furthermore, the re-dispersed Pt₁ is in different environment from the fresh Pt₁,³⁷ while fresh and re-dispersed Pd₁ are spectroscopically similar. On the other hand, TiO₂-R traps Pd₁ in surface O_v when reduced at 400 °C,²⁷ while TiO₂-A does not, because surface O_v is not thermodynamically favored on anatase.⁴⁹⁻⁵² The comparisons, along with the fact that the intrinsic activity increase is unique to Pd/TiO₂-A among all metal-support combinations (Figures 1c-d), emphasize that the dynamics of SACs are highly dependent on the properties of

the metal and the support, thus are difficult to generalize. The physical origin of the different behaviors of other metal-support pairs could be a topic of future studies.

Conclusions

This manuscript discussed the dynamic changes in the coordination environment and nuclearity of Pd₁ on anatase TiO₂ under conditions related to the rWGS, and their catalytic consequences. At $T \geq 350$ °C, the rWGS rate increases with TOS, which is unique to Pd₁ on TiO₂-A. The activation is driven by H₂ in the reaction stream, while the CO product deactivates the catalyst. *In-situ/operando* XAS revealed that the bulk reduction of TiO₂ by H₂ or the reaction stream partially cleaves the Pd–O interface and modifies the electronic structure of Pd. The new coordination environment of Pd sites facilitates rWGS turnover through the carboxyl pathway, which overcomes the minor sintering of some Pd₁ into disordered, flattened Pd_n of $d \approx 1$ nm. Such changes in Pd coordination environment is reversed under air, which at 400 °C, also re-disperses Pd_n into Pd₁, and promotes both the rWGS turnover and TiO₂ reduction by removing the auto-adsorbed carboxylate layers on TiO₂. On the other hand, the deactivation by CO is due to Pd₁ sintering into crystalline Pd_{NP} of $d \approx 5$ nm. This work elucidates the complicated dynamics of Pd₁/TiO₂ under pre-treatment and *operando* conditions, enhancing the fundamental understanding of SACs. It reveals the unique metal coordination environment leading to high intrinsic rWGS activity, establishing the instructive but often elusive structure-function relationship on SACs.

Supporting Information

Experimental methods; supplemental characterization data and related analysis (IR, XAS, XPS, TEM); supplemental rWGS kinetic data; kinetic modelling of Pd evolution under H₂; supplemental structural information from simulation (DFT and MD); typical kinetic parameters for the two rWGS reaction pathways

Acknowledgement

This work was supported by the U.S. Department of Energy, Office of Science, Basic Energy Sciences, Chemical Sciences, Geosciences, and Biosciences Division, Catalysis Science program, FWP 47319. PNNL is a multi-program national laboratory operated for DOE by Battelle. We acknowledge Dr. Mark E. Bowden, Ms. X. Shari Li, Mr. Mark Engelhard, and Dr. Yiqing Wu at PNNL for XRD, BET, XPS measurements, and material synthesis. Use of the Stanford Synchrotron Radiation Lightsource, SLAC National Accelerator Laboratory, is supported by the U.S. Department of Energy, Office of Science, Office of Basic Energy Sciences under Contract No. DE-AC02-76SF00515. This research used resources of the National Energy Research Scientific Computing Center, a DOE Office of Science User Facility supported by the Office of Science of the U.S. Department of Energy under Contract No. DE-AC02-05CH11231. Co-ACCESS is supported by the U.S. Department of Energy, Office of Basic Energy Sciences, Chemical Sciences, Geosciences and Bioscience Division. This research used resources of the Advanced Photon Source (APS), an Office of Science User Facility operated for the U.S. Department of Energy (DOE) Office of Science by Argonne National Laboratory, and was supported by the U.S. DOE under Contract No. DE-AC02-06CH11357, and the Canadian Light Source and its funding partners.

Reference

- (1) Li, Z.; Ji, S.; Liu, Y.; Cao, X.; Tian, S.; Chen, Y.; Niu, Z.; Li, Y. Well-Defined Materials for Heterogeneous Catalysis: From Nanoparticles to Isolated Single-Atom Sites. *Chem. Rev.* **2020**, *120* (2), 623-682.
- (2) Cui, X.; Li, W.; Ryabchuk, P.; Junge, K.; Beller, M. Bridging homogeneous and heterogeneous catalysis by heterogeneous single-metal-site catalysts. *Nat. Catal.* **2018**, *1* (6), 385-397.
- (3) Chen, Y.; Huang, Z.; Ma, Z.; Chen, J.; Tang, X. Fabrication, characterization, and stability of supported single-atom catalysts. *Catal. Sci. Technol.* **2017**, *7* (19), 4250-4258.
- (4) Liu, P.; Zhao, Y.; Qin, R.; Mo, S.; Chen, G.; Gu, L.; Chevrier, D. M.; Zhang, P.; Guo, Q.; Zang, D.; et al. Photochemical route for synthesizing atomically dispersed palladium catalysts. *Science* **2016**, *352* (6287), 797-800.
- (5) Jones, J.; Xiong, H.; DeLaRiva, A. T.; Peterson, E. J.; Pham, H.; Challa, S. R.; Qi, G.; Oh, S.; Wiebenga, M. H.; Pereira Hernández, X. I.; et al. Thermally stable single-atom platinum-on-ceria catalysts via atom trapping. *Science* **2016**, *353* (6295), 150-154.
- (6) Piernavieja-Hermida, M.; Lu, Z.; White, A.; Low, K.-B.; Wu, T.; Elam, J. W.; Wu, Z.; Lei, Y. Towards ALD thin film stabilized single-atom Pd1 catalysts. *Nanoscale* **2016**, *8* (33), 15348-15356.
- (7) Jiao, L.; Regalbuto, J. R. The synthesis of highly dispersed noble and base metals on silica via strong electrostatic adsorption: I. Amorphous silica. *J. Catal.* **2008**, *260* (2), 329-341.
- (8) Chen, L.; Sterbinsky, G. E.; Tait, S. L. Synthesis of platinum single-site centers through metal-ligand self-assembly on powdered metal oxide supports. *J. Catal.* **2018**, *365*, 303-312.
- (9) Li, X.; Yang, X.; Zhang, J.; Huang, Y.; Liu, B. In Situ/Operando Techniques for Characterization of Single-Atom Catalysts. *ACS Catal.* **2019**, *9* (3), 2521-2531.
- (10) Li, Y.; Frenkel, A. I. Deciphering the Local Environment of Single-Atom Catalysts with X-ray Absorption Spectroscopy. *Acc. Chem. Res.* **2021**, *54* (11), 2660-2669.
- (11) Asokan, C.; DeRita, L.; Christopher, P. Using probe molecule FTIR spectroscopy to identify and characterize Pt-group metal based single atom catalysts. *Chin. J. Catal.* **2017**, *38* (9), 1473-1480.
- (12) Kyriakou, G.; Boucher, M. B.; Jewell, A. D.; Lewis, E. A.; Lawton, T. J.; Baber, A. E.; Tierney, H. L.; Flytzani-Stephanopoulos, M.; Sykes, E. C. H. Isolated Metal Atom Geometries as a Strategy for Selective Heterogeneous Hydrogenations. *Science* **2012**, *335* (6073), 1209-1212.
- (13) DeRita, L.; Dai, S.; Lopez-Zepeda, K.; Pham, N.; Graham, G. W.; Pan, X.; Christopher, P. Catalyst Architecture for Stable Single Atom Dispersion Enables Site-Specific Spectroscopic and Reactivity Measurements of CO Adsorbed to Pt Atoms, Oxidized Pt Clusters, and Metallic Pt Clusters on TiO₂. *J. Am. Chem. Soc.* **2017**, *139* (40), 14150-14165.
- (14) Chen, L.; Ali, I. S.; Sterbinsky, G. E.; Gamler, J. T. L.; Skrabalak, S. E.; Tait, S. L. Alkene Hydrosilylation on Oxide-Supported Pt-Ligand Single-Site Catalysts. *ChemCatChem* **2019**, *11* (12), 2843-2854.
- (15) Chen, Z.; Vorobyeva, E.; Mitchell, S.; Fako, E.; Ortuño, M. A.; López, N.; Collins, S. M.; Midgley, P. A.; Richard, S.; Vilé, G.; et al. A heterogeneous single-atom palladium catalyst surpassing homogeneous systems for Suzuki coupling. *Nat. Nanotechnol.* **2018**, *13* (8), 702-707.
- (16) Macino, M.; Barnes, A. J.; Althabhan, S. M.; Qu, R.; Gibson, E. K.; Morgan, D. J.; Freakley, S. J.; Dimitratos, N.; Kiely, C. J.; Gao, X.; et al. Tuning of catalytic sites in Pt/TiO₂

- catalysts for the chemoselective hydrogenation of 3-nitrostyrene. *Nat. Catal.* **2019**, 2 (10), 873-881.
- (17) Chen, L.; Ali, I. S.; Sterbinsky, G. E.; Zhou, X.; Wasim, E.; Tait, S. L. Ligand-coordinated Ir single-atom catalysts stabilized on oxide supports for ethylene hydrogenation and their evolution under a reductive atmosphere. *Catal. Sci. Technol.* **2021**, 11 (6), 2081-2093.
- (18) Malta, G.; Freakley, S. J.; Kondrat, S. A.; Hutchings, G. J. Acetylene hydrochlorination using Au/carbon: a journey towards single site catalysis. *Chem. Comm.* **2017**, 53 (86), 11733-11746.
- (19) Yang, M.; Liu, J.; Lee, S.; Zugic, B.; Huang, J.; Allard, L. F.; Flytzani-Stephanopoulos, M. A Common Single-Site Pt(II)-O(OH)_x- Species Stabilized by Sodium on “Active” and “Inert” Supports Catalyzes the Water-Gas Shift Reaction. *J. Am. Chem. Soc.* **2015**, 137 (10), 3470-3473.
- (20) Ding, K.; Gulec, A.; Johnson, A. M.; Schweitzer, N. M.; Stucky, G. D.; Marks, L. D.; Stair, P. C. Identification of active sites in CO oxidation and water-gas shift over supported Pt catalysts. *Science* **2015**, 350 (6257), 189-192.
- (21) Wang, Y.-G.; Mei, D.; Glezakou, V.-A.; Li, J.; Rousseau, R. Dynamic formation of single-atom catalytic active sites on ceria-supported gold nanoparticles. *Nat. Comm.* **2015**, 6 (1), 6511.
- (22) Huang, F.; Deng, Y.; Chen, Y.; Cai, X.; Peng, M.; Jia, Z.; Ren, P.; Xiao, D.; Wen, X.; Wang, N.; et al. Atomically Dispersed Pd on Nanodiamond/Graphene Hybrid for Selective Hydrogenation of Acetylene. *J. Am. Chem. Soc.* **2018**, 140 (41), 13142-13146.
- (23) Tang, Y.; Asokan, C.; Xu, M.; Graham, G. W.; Pan, X.; Christopher, P.; Li, J.; Sautet, P. Rh single atoms on TiO₂ dynamically respond to reaction conditions by adapting their site. *Nat. Comm.* **2019**, 10 (1), 4488.
- (24) Daelman, N.; Capdevila-Cortada, M.; López, N. Dynamic charge and oxidation state of Pt/CeO₂ single-atom catalysts. *Nat. Mater.* **2019**, 18 (11), 1215-1221.
- (25) Li, H.; Wang, M.; Luo, L.; Zeng, J. Static Regulation and Dynamic Evolution of Single-Atom Catalysts in Thermal Catalytic Reactions. *Adv. Sci.* **2019**, 6 (3), 1801471.
- (26) Hu, P.; Huang, Z.; Amghouz, Z.; Makkee, M.; Xu, F.; Kapteijn, F.; Dikhtiarenko, A.; Chen, Y.; Gu, X.; Tang, X. Electronic Metal-Support Interactions in Single-Atom Catalysts. *Angew. Chem. Int. Ed.* **2014**, 53 (13), 3418-3421.
- (27) Nelson, N. C.; Chen, L.; Meira, D.; Kovarik, L.; Szanyi, J. In Situ Dispersion of Palladium on TiO₂ During Reverse Water-Gas Shift Reaction: Formation of Atomically Dispersed Palladium. *Angew. Chem. Int. Ed.* **2020**, 59 (40), 17657-17663.
- (28) DeRita, L.; Resasco, J.; Dai, S.; Boubnov, A.; Thang, H. V.; Hoffman, A. S.; Ro, I.; Graham, G. W.; Bare, S. R.; Pacchioni, G.; et al. Structural evolution of atomically dispersed Pt catalysts dictates reactivity. *Nat. Mater.* **2019**, 18 (7), 746-751.
- (29) Muravev, V.; Spezzati, G.; Su, Y.-Q.; Parastaev, A.; Chiang, F.-K.; Longo, A.; Escudero, C.; Kosinov, N.; Hensen, E. J. M. Interface dynamics of Pd-CeO₂ single-atom catalysts during CO oxidation. *Nat. Catal.* **2021**, 4 (6), 469-478.
- (30) Gates, B. C.; Flytzani-Stephanopoulos, M.; Dixon, D. A.; Katz, A. Atomically dispersed supported metal catalysts: perspectives and suggestions for future research. *Catal. Sci. Technol.* **2017**, 7 (19), 4259-4275.
- (31) Hoffman, A. S.; Debeve, L. M.; Zhang, S.; Perez-Aguilar, J. E.; Conley, E. T.; Justl, K. R.; Arslan, I.; Dixon, D. A.; Gates, B. C. Beating Heterogeneity of Single-Site Catalysts: MgO-Supported Iridium Complexes. *ACS Catal.* **2018**, 8 (4), 3489-3498.

- (32) Hoffman, A. S.; Fang, C.-Y.; Gates, B. C. Homogeneity of Surface Sites in Supported Single-Site Metal Catalysts: Assessment with Band Widths of Metal Carbonyl Infrared Spectra. *J. Phys. Chem. Lett.* **2016**, 7 (19), 3854-3860.
- (33) Doudin, N.; Yuk, S. F.; Marcinkowski, M. D.; Nguyen, M.-T.; Liu, J.-C.; Wang, Y.; Novotny, Z.; Kay, B. D.; Li, J.; Glezakou, V.-A.; et al. Understanding Heterolytic H₂ Cleavage and Water-Assisted Hydrogen Spillover on Fe₃O₄(001)-Supported Single Palladium Atoms. *ACS Catal.* **2019**, 9 (9), 7876-7887.
- (34) Bliem, R.; van der Hoeven, J.; Zavodny, A.; Gamba, O.; Pavelec, J.; de Jongh, P. E.; Schmid, M.; Diebold, U.; Parkinson, G. S. An Atomic-Scale View of CO and H₂ Oxidation on a Pt/Fe₃O₄ Model Catalyst. *Angew. Chem. Int. Ed.* **2015**, 54 (47), 13999-14002.
- (35) Parkinson, G. S.; Novotny, Z.; Argentero, G.; Schmid, M.; Pavelec, J.; Kosak, R.; Blaha, P.; Diebold, U. Carbon monoxide-induced adatom sintering in a Pd–Fe₃O₄ model catalyst. *Nat. Mater.* **2013**, 12 (8), 724-728.
- (36) Wang, H.; Liu, J.-X.; Allard, L. F.; Lee, S.; Liu, J.; Li, H.; Wang, J.; Wang, J.; Oh, S. H.; Li, W.; et al. Surpassing the single-atom catalytic activity limit through paired Pt-O-Pt ensemble built from isolated Pt₁ atoms. *Nat. Comm.* **2019**, 10 (1), 3808.
- (37) Chen, L.; Unocic, R. R.; Hoffman, A. S.; Hong, J.; Braga, A. H.; Bao, Z.; Bare, S. R.; Szanyi, J. Unlocking the Catalytic Potential of TiO₂-Supported Pt Single Atoms for the Reverse Water–Gas Shift Reaction by Altering Their Chemical Environment. *JACS Au* **2021**, 1 (7), 977-986.
- (38) Asokan, C.; Thang, H. V.; Pacchioni, G.; Christopher, P. Reductant composition influences the coordination of atomically dispersed Rh on anatase TiO₂. *Catal. Sci. Technol.* **2020**, 10 (6), 1597-1601.
- (39) Nelson, N. C.; Nguyen, M.-T.; Glezakou, V.-A.; Rousseau, R.; Szanyi, J. Carboxyl intermediate formation via an in situ-generated metastable active site during water-gas shift catalysis. *Nat. Catal.* **2019**, 2 (10), 916-924.
- (40) Wu, H. C.; Chang, Y. C.; Wu, J. H.; Lin, J. H.; Lin, I. K.; Chen, C. S. Methanation of CO₂ and reverse water gas shift reactions on Ni/SiO₂ catalysts: the influence of particle size on selectivity and reaction pathway. *Catal. Sci. Technol.* **2015**, 5 (8), 4154-4163.
- (41) Wang, L. C.; Tahvildar Khazaneh, M.; Widmann, D.; Behm, R. J. TAP reactor studies of the oxidizing capability of CO₂ on a Au/CeO₂ catalyst – A first step toward identifying a redox mechanism in the Reverse Water–Gas Shift reaction. *J. Catal.* **2013**, 302, 20-30.
- (42) Rodriguez, J. A.; Evans, J.; Feria, L.; Vidal, A. B.; Liu, P.; Nakamura, K.; Illas, F. CO₂ hydrogenation on Au/TiC, Cu/TiC, and Ni/TiC catalysts: Production of CO, methanol, and methane. *J. Catal.* **2013**, 307, 162-169.
- (43) Erdöhelyi, A.; Pásztor, M.; Solymosi, F. Catalytic hydrogenation of CO₂ over supported palladium. *J. Catal.* **1986**, 98 (1), 166-177.
- (44) Nelson, N. C.; Szanyi, J. Heterolytic Hydrogen Activation: Understanding Support Effects in Water–Gas Shift, Hydrodeoxygenation, and CO Oxidation Catalysis. *ACS Catal.* **2020**, 10, 5663-5671.
- (45) Kwak, J. H.; Kovarik, L.; Szanyi, J. Heterogeneous Catalysis on Atomically Dispersed Supported Metals: CO₂ Reduction on Multifunctional Pd Catalysts. *ACS Catal.* **2013**, 3 (9), 2094-2100.
- (46) Kwak, J. H.; Kovarik, L.; Szanyi, J. CO₂ Reduction on Supported Ru/Al₂O₃ Catalysts: Cluster Size Dependence of Product Selectivity. *ACS Catal.* **2013**, 3 (11), 2449-2455.

- (47) Matsubu, J. C.; Yang, V. N.; Christopher, P. Isolated Metal Active Site Concentration and Stability Control Catalytic CO₂ Reduction Selectivity. *J. Am. Chem. Soc.* **2015**, *137* (8), 3076-3084.
- (48) Patra, S.; Davoisne, C.; Bouyanfif, H.; Foix, D.; Sauvage, F. Phase stability frustration on ultra-nanosized anatase TiO₂. *Sci. Rep.* **2015**, *5* (1), 10928.
- (49) Di Valentin, C.; Pacchioni, G.; Selloni, A. Reduced and n-Type Doped TiO₂: Nature of Ti³⁺ Species. *J. Phys. Chem. C* **2009**, *113* (48), 20543-20552.
- (50) Cheng, H.; Selloni, A. Surface and subsurface oxygen vacancies in anatase TiO₂ and differences with rutile. *Phys. Rev. B* **2009**, *79* (9), 092101.
- (51) Cheng, H.; Selloni, A. Energetics and diffusion of intrinsic surface and subsurface defects on anatase TiO₂(101). *J. Chem. Phys.* **2009**, *131* (5), 054703.
- (52) Islam, M. M.; Calatayud, M.; Pacchioni, G. Hydrogen Adsorption and Diffusion on the Anatase TiO₂(101) Surface: A First-Principles Investigation. *J. Phys. Chem. C* **2011**, *115* (14), 6809-6814.
- (53) Diebold, U. The surface science of titanium dioxide. *Surf. Sci. Rep.* **2003**, *48* (5), 53-229.
- (54) Zhang, H.; F. Banfield, J. Thermodynamic analysis of phase stability of nanocrystalline titania. *J. Mater. Chem.* **1998**, *8* (9), 2073-2076.
- (55) Hadjiivanov, K. I.; Klissurski, D. G. Surface chemistry of titania (anatase) and titania-supported catalysts. *Chem. Soc. Rev.* **1996**, *25* (1), 61-69.
- (56) Wolter, K.; Seiferth, O.; Libuda, J.; Kuhlenbeck, H.; Bäumer, M.; Freund, H. J. Infrared study of CO adsorption on alumina supported palladium particles. *Surf. Sci.* **1998**, *402-404*, 428-432.
- (57) Bensalem, A.; Muller, J.-C.; Tessier, D.; Bozon-Verduraz, F. Spectroscopic study of CO adsorption on palladium–ceria catalysts. *J. Chem. Soc., Faraday Trans.* **1996**, *92* (17), 3233-3237.
- (58) Tessier, D.; Rakai, A.; Bozon-Verduraz, F. Spectroscopic study of the interaction of carbon monoxide with cationic and metallic palladium in palladium–alumina catalysts. *J. Chem. Soc., Faraday Trans.* **1992**, *88* (5), 741-749.
- (59) Vannice, M. A.; Wang, S. Y. Determination of IR extinction coefficients for linear- and bridged-bonded carbon monoxide on supported palladium. *J. Phys. Chem.* **1981**, *85* (17), 2543-2546.
- (60) Jentys, A. Estimation of mean size and shape of small metal particles by EXAFS. *Phys. Chem. Chem. Phys.* **1999**, *1* (17), 4059-4063.
- (61) Vaarkamp, M.; Modica, F. S.; Miller, J. T.; Koningsberger, D. C. Influence of Hydrogen Pretreatment on the Structure of the Metal-Support Interface in Pt/Zelite Catalysts. *J. Catal.* **1993**, *144* (2), 611-626.
- (62) Koningsberger, D. C.; Gates, B. C. Nature of the metal-support interface in supported metal catalysts: Results from X-ray absorption spectroscopy. *Catal. Lett.* **1992**, *14* (3), 271-277.
- (63) Moller, K.; Koningsberger, D. C.; Bein, T. Stabilization of metal ensembles at room temperature: palladium clusters in zeolites. *J. Phys. Chem.* **1989**, *93* (16), 6116-6120.
- (64) Martens, J. H. A.; Prins, R.; Zandbergen, H.; Koningsberger, D. C. Structure of rhodium/titania in the normal and the SMSI state as determined by extended x-ray absorption fine structure and high-resolution transmission electron microscopy. *J. Phys. Chem.* **1988**, *92* (7), 1903-1916.
- (65) Koningsberger, D. C.; Sayers, D. E. An EXAFS study of platinum - oxygen bonds in the metal-support interface of a highly dispersed Pt/Al₂O₃ catalyst. *Solid State Ion.* **1985**, *16*, 23-27.

- (66) Van't Blik, H. F. J.; Van Zon, J. B. A. D.; Huizinga, T.; Vis, J. C.; Koningsberger, D. C.; Prins, R. Structure of rhodium in an ultradispersed rhodium/alumina catalyst as studied by EXAFS and other techniques. *J. Am. Chem. Soc.* **1985**, *107* (11), 3139-3147.
- (67) Koningsberger, D. C.; Van Zon, J. B. A. D.; Van't Blik, H. F. J.; Visser, G. J.; Prins, R.; Mansour, A. N.; Sayers, D. E.; Short, D. R.; Katzer, J. R. An extended x-ray absorption fine structure study of rhodium-oxygen bonds in a highly dispersed rhodium/aluminum oxide catalyst. *J. Phys. Chem.* **1985**, *89* (19), 4075-4081.
- (68) Bond, G. C.; Coq, B.; Dutartre, R.; Ruiz, J. G.; Hooper, A. D.; Proietti, M. G.; Sierra, M. C. S.; Slaa, J. C. Effect of Various Pretreatments on the Structure and Properties of Ruthenium Catalysts. *J. Catal.* **1996**, *161* (1), 480-494.
- (69) Zaki, M. I.; Kunzmann, G.; Gates, B. C.; Knoezinger, H. Highly dispersed rhodium on alumina catalysts: influence of the atmosphere on the state and dispersion of rhodium. *J. Phys. Chem.* **1987**, *91* (6), 1486-1493.
- (70) Jin, C.; Dai, Y.; Wei, W.; Ma, X.; Li, M.; Huang, B. Effects of single metal atom (Pt, Pd, Rh and Ru) adsorption on the photocatalytic properties of anatase TiO₂. *Appl. Surf. Sci.* **2017**, *426*, 639-646.
- (71) Hasan, M. A.; Zaki, M. I.; Pasupulety, L. Oxide-catalyzed conversion of acetic acid into acetone: an FTIR spectroscopic investigation. *Appl. Catal., A* **2003**, *243* (1), 81-92.
- (72) Pei, Z. F.; Ponec, V. On the intermediates of the acetic acid reactions on oxides: an IR study. *Appl. Surf. Sci.* **1996**, *103* (2), 171-182.
- (73) Mattsson, A.; Österlund, L. Adsorption and Photoinduced Decomposition of Acetone and Acetic Acid on Anatase, Brookite, and Rutile TiO₂ Nanoparticles. *J. Phys. Chem. C* **2010**, *114* (33), 14121-14132.
- (74) Sun, Z.; Kong, L.; Ding, X.; Du, C.; Zhao, X.; Chen, J.; Fu, H.; Yang, X.; Cheng, T. The effects of acetaldehyde, glyoxal and acetic acid on the heterogeneous reaction of nitrogen dioxide on gamma-alumina. *Phys. Chem. Chem. Phys.* **2016**, *18* (14), 9367-9376.
- (75) Backes, M. J.; Lukaski, A. C.; Muggli, D. S. Active sites and effects of H₂O and temperature on the photocatalytic oxidation of ¹³C-acetic acid on TiO₂. *Appl. Catal., B* **2005**, *61* (1), 21-35.
- (76) Balajka, J.; Hines, M. A.; DeBenedetti, W. J. I.; Komora, M.; Pavelec, J.; Schmid, M.; Diebold, U. High-affinity adsorption leads to molecularly ordered interfaces on TiO₂ in air and solution. *Science* **2018**, *361* (6404), 786-789.
- (77) Khare, P.; Kumar, N.; Kumari, K. M.; Srivastava, S. S. Atmospheric formic and acetic acids: An overview. *Rev. Geophys.* **1999**, *37* (2), 227-248.
- (78) Grinter, D. C.; Nicotra, M.; Thornton, G. Acetic Acid Adsorption on Anatase TiO₂(101). *J. Phys. Chem. C* **2012**, *116* (21), 11643-11651.
- (79) Chen, L.; Kovarik, L.; Szanyi, J. Temperature-Dependent Communication between Pt/Al₂O₃ Catalysts and Anatase TiO₂ Dilutant: the Effects of Metal Migration and Carbon Transfer on the Reverse Water–Gas Shift Reaction. *ACS Catal.* **2021**, *11* (19), 12058-12067.
- (80) Whittaker, T.; Kumar, K. B. S.; Peterson, C.; Pollock, M. N.; Grabow, L. C.; Chandler, B. D. H₂ Oxidation over Supported Au Nanoparticle Catalysts: Evidence for Heterolytic H₂ Activation at the Metal–Support Interface. *J. Am. Chem. Soc.* **2018**, *140* (48), 16469-16487.
- (81) Panayotov, D. A.; Yates, J. T. Spectroscopic Detection of Hydrogen Atom Spillover from Au Nanoparticles Supported on TiO₂: Use of Conduction Band Electrons. *J. Phys. Chem. C* **2007**, *111* (7), 2959-2964.

- (82) Mahdavi-Shakib, A.; Kumar, K. B. S.; Whittaker, T. N.; Xie, T.; Grabow, L. C.; Rioux, R. M.; Chandler, B. D. Kinetics of H₂ Adsorption at the Metal–Support Interface of Au/TiO₂ Catalysts Probed by Broad Background IR Absorbance. *Angew. Chem. Int. Ed.* **2021**, *60* (14), 7735-7743.
- (83) Wang, X.; Shi, H.; Szanyi, J. Controlling selectivities in CO₂ reduction through mechanistic understanding. *Nat. Comm.* **2017**, *8* (1), 513.
- (84) Wang, X.; Hong, Y.; Shi, H.; Szanyi, J. Kinetic modeling and transient DRIFTS–MS studies of CO₂ methanation over Ru/Al₂O₃ catalysts. *J. Catal.* **2016**, *343*, 185-195.
- (85) Wang, X.; Shi, H.; Kwak, J. H.; Szanyi, J. Mechanism of CO₂ Hydrogenation on Pd/Al₂O₃ Catalysts: Kinetics and Transient DRIFTS-MS Studies. *ACS Catal.* **2015**, *5* (11), 6337-6349.
- (86) Lu, J.; Aydin, C.; Browning, N. D.; Gates, B. C. Oxide- and Zeolite-Supported Isostructural Ir(C₂H₄)₂ Complexes: Molecular-Level Observations of Electronic Effects of Supports as Ligands. *Langmuir* **2012**, *28* (35), 12806-12815.
- (87) Lu, J.; Serna, P.; Gates, B. C. Zeolite- and MgO-Supported Molecular Iridium Complexes: Support and Ligand Effects in Catalysis of Ethene Hydrogenation and H–D Exchange in the Conversion of H₂ + D₂. *ACS Catal.* **2011**, *1* (11), 1549-1561.
- (88) Babucci, M.; Fang, C.-Y.; Hoffman, A. S.; Bare, S. R.; Gates, B. C.; Uzun, A. Tuning the Selectivity of Single-Site Supported Metal Catalysts with Ionic Liquids. *ACS Catal.* **2017**, *7* (10), 6969-6972.
- (89) Abdel-Mageed, A. M.; Wiese, K.; Hauble, A.; Bansmann, J.; Rabeah, J.; Parlinska-Wojtan, M.; Brückner, A.; Behm, R. J. Steering the selectivity in CO₂ reduction on highly active Ru/TiO₂ catalysts: Support particle size effects. *J. Catal.* **2021**, *401*, 160-173.
- (90) Chen, S.; Abdel-Mageed, A. M.; Mochizuki, C.; Ishida, T.; Murayama, T.; Rabeah, J.; Parlinska-Wojtan, M.; Brückner, A.; Behm, R. J. Controlling the O-Vacancy Formation and Performance of Au/ZnO Catalysts in CO₂ Reduction to Methanol by the ZnO Particle Size. *ACS Catal.* **2021**, *11* (15), 9022-9033.
- (91) Abdel-Mageed, A. M.; Klyushin, A.; Rezvani, A.; Knop-Gericke, A.; Schlögl, R.; Behm, R. J. Negative Charging of Au Nanoparticles during Methanol Synthesis from CO₂/H₂ on a Au/ZnO Catalyst: Insights from Operando IR and Near-Ambient-Pressure XPS and XAS Measurements. *Angew. Chem. Int. Ed.* **2019**, *58* (30), 10325-10329.
- (92) Abdel-Mageed, A. M.; Klyushin, A.; Knop-Gericke, A.; Schlögl, R.; Behm, R. J. Influence of CO on the Activation, O-Vacancy Formation, and Performance of Au/ZnO Catalysts in CO₂ Hydrogenation to Methanol. *J. Phys. Chem. Lett.* **2019**, *10* (13), 3645-3653.
- (93) Wang, Y.; Widmann, D.; Behm, R. J. Influence of TiO₂ Bulk Defects on CO Adsorption and CO Oxidation on Au/TiO₂: Electronic Metal–Support Interactions (EMSI) in Supported Au Catalysts. *ACS Catal.* **2017**, *7* (4), 2339-2345.
- (94) Kelly, S. D.; Charochak, M. E.; Blackwell, N.; Bare, S. R. EXAFS Model of 2-Dimensional Platinum Clusters. *J. Phys. Conf. Ser.* **2013**, *430*, 012061.
- (95) Roldan Cuenya, B.; Alcántara Ortigoza, M.; Ono, L. K.; Behafarid, F.; Mostafa, S.; Croy, J. R.; Paredis, K.; Shafai, G.; Rahman, T. S.; Li, L.; et al. Thermodynamic properties of Pt nanoparticles: Size, shape, support, and adsorbate effects. *Phys. Rev. B* **2011**, *84* (24), 245438.
- (96) Chen, L.; Meyer, L. C.; Kovarik, L.; Meira, D.; Pereira-Hernandez, X. I.; Shi, H.; Khivantsev, K.; Gutiérrez, O. Y.; Szanyi, J. Disordered, Sub-Nanometer Ru Structures on CeO₂ are Highly Efficient and Selective Catalysts in Polymer Upcycling by Hydrogenolysis. *ACS Catal.* **2022**, *12* (8), 4618-4627.

- (97) Shao, X.; Prada, S.; Giordano, L.; Pacchioni, G.; Nilius, N.; Freund, H.-J. Tailoring the Shape of Metal Ad-Particles by Doping the Oxide Support. *Angew. Chem. Int. Ed.* **2011**, *50* (48), 11525-11527.
- (98) Risse, T.; Shaikhutdinov, S.; Nilius, N.; Sterrer, M.; Freund, H.-J. Gold Supported on Thin Oxide Films: From Single Atoms to Nanoparticles. *Acc. Chem. Res.* **2008**, *41* (8), 949-956.
- (99) Sterrer, M.; Risse, T.; Heyde, M.; Rust, H.-P.; Freund, H.-J. Crossover from Three-Dimensional to Two-Dimensional Geometries of Au Nanostructures on Thin MgO(001) Films: A Confirmation of Theoretical Predictions. *Phys. Rev. Lett.* **2007**, *98* (20), 206103.
- (100) Lemire, C.; Meyer, R.; Shaikhutdinov, S. K.; Freund, H. J. CO adsorption on oxide supported gold: from small clusters to monolayer islands and three-dimensional nanoparticles. *Surf. Sci.* **2004**, *552* (1), 27-34.
- (101) Kwak, J. H.; Hu, J.; Mei, D.; Yi, C.-W.; Kim, D. H.; Peden, C. H. F.; Allard, L. F.; Szanyi, J. Coordinatively Unsaturated Al³⁺ Centers as Binding Sites for Active Catalyst Phases of Platinum on γ -Al₂O₃. *Science* **2009**, *325* (5948), 1670-1673.
- (102) Scheiber, P.; Fidler, M.; Dulub, O.; Schmid, M.; Diebold, U.; Hou, W.; Aschauer, U.; Selloni, A. (Sub)Surface Mobility of Oxygen Vacancies at the TiO₂ Anatase (101) Surface. *Phys. Rev. Lett.* **2012**, *109* (13), 136103.
- (103) Alghannam, A.; Muhich, C. L.; Musgrave, C. B. Adatom surface diffusion of catalytic metals on the anatase TiO₂(101) surface. *Phys. Chem. Chem. Phys.* **2017**, *19* (6), 4541-4552.
- (104) Han, Y.; Liu, C.-j.; Ge, Q. Effect of Surface Oxygen Vacancy on Pt Cluster Adsorption and Growth on the Defective Anatase TiO₂(101) Surface. *J. Phys. Chem. C* **2007**, *111* (44), 16397-16404.

TOC Graphic:

